Ocean Dynamics
https://doi.org/10.1007/s10236-024-01611-0

Influence of the representation of landfast ice on the simulation of the Arctic sea ice and Arctic Ocean halocline

Jean Sterlin[1] · Tim Orval[1] · Jean-François Lemieux[2] · Clément Rousset[3] · Thierry Fichefet[1] · François Massonnet[1] · Jonathan Raulier[1]

Received: 12 December 2023 / Accepted: 21 March 2024

Abstract
Landfast ice is near-motionless sea ice attached to the coast. Despite its potential for modifying sea ice and ocean properties, most state-of-the-art sea ice models poorly represent landfast ice. Here, we examine two crucial processes responsible for the formation and stabilization of landfast ice, namely sea ice tensile strength and seabed–ice keel interactions. We investigate the impact of these processes on the Arctic sea ice cover and halocline layer using the global coupled ocean–sea ice model NEMO-LIM3. We show that including seabed–ice keel stress improves the seasonality and spatial distribution of the landfast ice cover in the Laptev and East Siberian Seas. This improved landfast ice representation sets the position of flaw polynyas to new locations approximately above the continental shelf break. The impact of sea ice tensile strength on the stability of the Arctic halocline layer is far more effective. Incorporating this process in the model yields a thicker, more consolidated, and less mobile Arctic sea ice pack that further decouples the ocean and atmosphere. As a result, the available potential energy of the Arctic halocline is decreased (increased) by $\sim$30kJ/m^2 ($\sim$30kJ/m^2) in the Amerasian (Eurasian) compared to the reference simulation excluding sea ice tensile strength and seabed–ice keel stress. Our findings highlight the need to better understand landfast ice physical processes conjointly with the subsequent influences on the ocean and sea ice states.

Keywords Arctic landfast ice · Arctic Ocean halocline · Available potential energy · Sea ice model · Ocean general circulation model

1 Introduction

Arctic sea ice strongly modifies the heat, momentum, and mass exchanges between the atmosphere and the Arctic Ocean, with far-reaching effects on the global climate (Bourassa et al. 2013). However, Arctic sea ice has become thinner (Kwok 2018), younger (Maslanik et al. 2011), smaller in extent (Serreze and Meier 2018), and more mobile (Rampal et al. 2009; Tandon et al. 2018; Lipatov et al. 2021) since the late 1970s. We expect these changes to continue in the coming decades (Haine and Martin 2017) as Arctic sea ice is transitioning towards a seasonally ice-free state (Meredith et al. 2019).

The Arctic halocline layer is a second barrier, limiting the interactions between Arctic sea ice and the Arctic Ocean. This layer lies between the surface mixed layer and the Atlantic waters of the Arctic Ocean. The Arctic halocline restricts thermally driven deep convection, enabling sea ice to grow over deep waters (Untersteiner 1975). Three main mechanisms have been suggested to explain the formation of the Arctic halocline: 1) salinification of the cold and fresh surface water under sea ice; 2) horizontal advection of cold and saline continental shelf waters; 3) modified Atlantic waters due to the melting of sea ice in the ice-covered Arctic shelves

Responsible Editor: Jia Wang

Tim Orval, Jean-François Lemieux, Clément Rousset, Thierry Fichefet, François Massonnet, and Jonathan Raulier these author's contributed equally to this work

✉ Jean Sterlin
jean.sterlin@uclouvain.be

1 Earth and Life Institute, Université Catholique de Louvain, Louvain-la-Neuve 1348, Belgium

2 Recherche en Prévision Numérique Environnementale, Environnement et Changement Climatique Canada, Dorval, Québec, Canada

3 Laboratoire d'Océanographie et du Climat : Expérimentations et Approches Numériques, Institut Pierre-Simon Laplace, 4 place de Jussieu, Paris 75005, France

Published online: 11 April 2024

(Metzner et al. 2020). Observations indicate an erosion of the Arctic halocline in the Eurasian Basin (Steele and Boyd 1998; Polyakov et al. 2017; Timmermans et al. 2018; Polyakov et al. 2020), concurrent with sea ice loss and increased ocean heat transport in the Arctic Basin (Årthun et al. 2012; Lind et al. 2018; Polyakov et al. 2017). The weakening of the Arctic halocline stratification facilitates the intrusion of Atlantic water into the surface mixed layer, promoting sea ice loss and atmosphere-ocean interactions (Årthun et al. 2012; Lind et al. 2018; Polyakov et al. 2017). This process describing the rising influence of Atlantic water on the Arctic Ocean is referred to as the "Atlantification" of the Arctic Ocean (e.g., Polyakov et al. 2017). In the coming decades, the influence of Atlantic water is expected to extend farther into the interior of the Arctic Ocean (Metzner et al. 2020; Årthun et al. 2019).

Landfast ice is the near motionless part of sea ice attached to the shore, to an ice wall (seaward margin of a glacier aground), to an ice front (seaward margin of a glacier afloat), between shoals or grounded icebergs (WMO 1970). Arctic landfast ice generally forms in early winter, reaches a maximum extent around April, and breaks up in June (Mahoney et al. 2014). It is commonly found in coastal regions of the Arctic, such as the Canadian Arctic Archipelago (CAA) or the shelf waters along Siberia (Fig. 1). The landfast ice edge can extend 100–200km offshore in the East Siberian Sea (Li et al. 2020). The landfast ice growth is mainly thermodynamically driven, limiting the mean thickness of this type of ice to ∼1.5m in most of the Arctic (Barry et al. 1979; Brown and Cote 1992; Li et al. 2020).

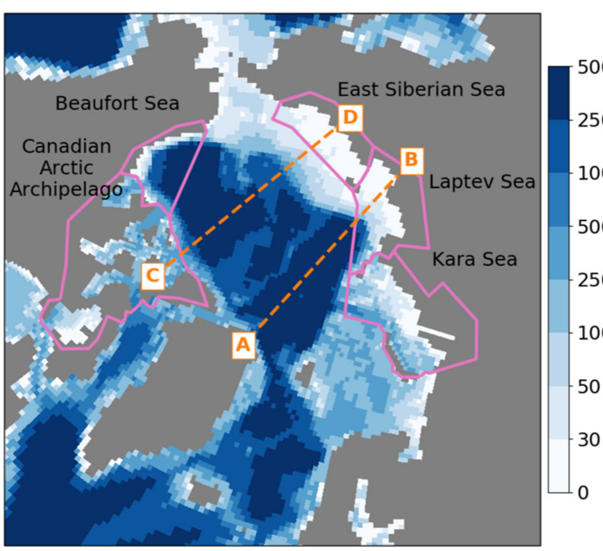

Fig. 1 Bathymetry (m) of the Arctic Ocean from our configuration of NEMO-LIM3. The purple boxes mark the regions used for the landfast ice analysis. The dashed orange lines indicate the oceanic transect positions used to assess the Arctic halocline stratification

Landfast ice acts as a buffer zone between drift ice and the coastline, consequently inhibiting the piling of sea ice due to convergent ice motion (Itkin et al. 2015). Moreover, the landfast ice cover shields the shelf water and river runoff from interactions with the atmosphere in winter (Itkin et al. 2015; Janout et al. 2020). Landfast ice sets the position of low sea ice concentration areas known as flaw polynyas (Dethleff et al. 1998; Morales Maqueda et al. 2004). These polynyas contribute significantly to the total sea ice volume produced in the Arctic (Tamura and Ohshima 2011; Iwamoto et al. 2014; Preußer et al. 2016). Freezing in flaw polynyas leads to the formation of dense waters in winter. Part of these dense waters feed into the Arctic halocline layer (Aagaard et al. 1981). As a result, Arctic landfast ice can influence the Arctic halocline (Itkin et al. 2015).

The modelling community has developed parameterizations targeting sea ice processes leading to the development of landfast ice in large-scale sea ice models. We can classify the most advanced of these parameterizations of landfast ice processes into two main groups. In the first group, a sea ice stress term is added to the momentum equation for sea ice to represent frictional forces between the sea ice keels and the seafloor. Lemieux et al. (2015) developed a basal stress parameterization, hereafter referred to as the seabed stress parameterization, to represent the effect of grounded ice keels on sea ice dynamics. Dupont et al. (2022) refined this formulation to account for the subgrid-scale variability of the sea ice thickness and ocean bathymetry. In addition, Huot (2021) and Van Achter et al. (2022) simulated Antarctic landfast ice in NEMO-LIM3 by prescribing grounded icebergs as masked land points. These masked land points act as anchoring platforms for landfast ice. In the second group, the sea ice rheology is modified to better account for the tensile strength properties of landfast ice. Olason (2016) and Dumont et al. (2009) showed that static ice arches are sustainable in models thanks to the uniaxial compressive strength property of the commonly used elliptical ice yield curve. König Beatty and Holland (2010) proposed to modify this yield curve to include isotropic tensile strength. Indeed, observations support evidence of a non-zero isotropic tensile strength for drift ice (Coon et al. 2007) and landfast ice (Tremblay and Hakakian 2006; König Beatty 2007). Itkin et al. (2015) simulated landfast ice in the Siberian shelf regions of the Arctic by prescribing positive isotropic tensile strength and increasing sea ice internal strength in shallow water areas. Later, Lemieux et al. (2016) improved the simulation of Arctic landfast ice by combining ice tensile strength (König Beatty and Holland 2010) with an ice grounding scheme based on a seabed stress parameterization (Lemieux et al. 2015). More recently, Liu et al. (2022) modified the no-slip lateral boundary condition in their sea ice model to include a coastal drag term. This term expresses the friction between sea ice and the coastline.

Today, the physical processes sustaining landfast are not yet fully understood. Seabed stress schemes improve the simulation of landfast ice in shallow seas (Lemieux et al. 2015). However, these schemes are suboptimal over deep waters, where ice ridges may not reach the seafloor (Lemieux et al. 2016; Dupont et al. 2022). On the other hand, Itkin et al. (2015) showed that prescribing positive tensile strength in shallow water regions may also improve the simulation of landfast ice in the Laptev and East Siberian Seas (LESS). Nonetheless, available observations poorly constrain the amount of isotropic and uniaxial ice tensile strengths (Coon et al. 2007). Liu et al. (2022) suggest including a coastal drag term in the ice momentum equation to improve the simulation of Arctic landfast ice. Tidal effects further complicate the modelling of landfast ice by increasing the ocean surface stress under sea ice thus dynamically weakening the stratification of the landfast ice cover (Lemieux et al. 2018).

Updating the tensile stress parameterization results in the modification of the rheology in the sea ice model; therefore, its impacts are not limited to landfast ice modelling, but also apply to the whole ice pack simulations more or less (Lemieux et al. 2016; Liu et al. 2022). Yet, these indirect effects on Arctic sea ice are not well known despite having the potential to influence the underlying polar ocean. Furthermore, Itkin et al. (2015) demonstrated the influence of Arctic landfast ice on the Arctic Ocean stratification from the surface down to 50m. The full extent of the impact of landfast ice on the Arctic Ocean stratification remains unknown. Additionally, most climate studies examining landfast ice processes rely on relatively high horizontal model resolutions and short periods of time for their analyses (e.g., Itkin et al. 2015; Lemieux et al. 2015; Olason 2016; Liu et al. 2022). It is unclear how current state-of-the-art landfast process schemes would perform using modest horizontal model resolutions ($\sim 1°$) and more than decade-long simulations.

The main objective of this study is to improve our understanding of the importance of landfast ice for the Arctic sea ice state and to determine the influence of this type of ice on the stability of the Arctic halocline. First, we implement the seabed stress parameterization of Lemieux et al. (2015) and the ice tensile strength formulation of König Beatty and Holland (2010) in our 1° horizontal resolution global ocean–sea ice model NEMO-LIM3. Next, we perform a series of sensitivity experiments of the Arctic landfast ice cover from 1980 to 2015 and compare the results to landfast ice observations based on the National Ice Center (NIC) sea ice charts (Fetterer and Fowler 2006; Dupont et al. 2022). Then, we examine the influence of those parameterizations on various characteristics of the Arctic sea ice cover simulated by the model. Finally, we evaluate the effects of the landfast ice process schemes on the stability of the Arctic halocline layer using the diagnostics introduced by Polyakov et al. (2018). In particular, we use the available potential energy (APE), which integrates potential density anomalies from the base of the Arctic halocline layer up to the sea surface. This diagnostic allows us to estimate the strength of the stratification of the Arctic halocline layer quantitatively over its entire thickness (e.g., Uotila et al. 2006).

Section 2 describes the ocean–sea ice modelling framework NEMO-LIM3, its global configuration, the implementation of the seabed stress and tensile strength schemes in NEMO-LIM3, the diagnostics used for assessing the Arctic halocline stability, and the experimental setup. Then, Section 3.1 presents a validation of the simulated Arctic landfast ice cover, mean sea ice state, and halocline layer. Next, the effects of the landfast ice process schemes on the Arctic mean sea ice state are examined in Section 3.2. The impact of these schemes on the Arctic Ocean is investigated in Section 3.3. Lastly, Section 4 provides concluding remarks.

2 Methods

2.1 Numerical models

In this study, we use the modelling framework Nucleus for European Modelling of the Ocean (NEMO), version 3.6 stable (SVN revision 7169), which couples the Océan PArallélisé (OPA) ocean model with the Louvain-la-Neuve sea ice model, version 3 (LIM3). OPA is a finite-difference, hydrostatic, primitive equation model using the Boussinesq approximation (Madec et al. 2017). The turbulent kinetic energy (TKE) closure model solves the vertical ocean eddy viscosity and diffusivity coefficients using a prognostic equation for the TKE and a closure assumption for the turbulent length scales (Blanke and Delecluse 1993; Madec et al. 2017). LIM3 is a state-of-the-art thermodynamic-dynamic sea ice model (Vancoppenolle et al. 2009; Rousset et al. 2015). This model features a discrete subgrid-scale ice thickness distribution (ITD) (Thorndike et al. 1975) configured with five ice categories. The boundaries of the thickness categories used in our simulations are 0, 0.45, 1.13, 2.14, 3.67 and 99m (Massonnet et al. 2019, see Eq. 2). The formulations of Bitz and Lipscomb (1999) and Vancoppenolle et al. (2007) solve the vertical sea ice thermodynamics for each ice category using five layers of ice and one of snow. The second-order moment-conserving scheme of Prather (1986) advects the sea ice and snow properties for each thickness category. The modelling of the ice interactions is based on the viscous-plastic rheology with an elliptical yield curve (Hibler 1979). This rheology is solved by iteration using the elastic-viscous-plastic (EVP) method (Hunke and Dukowicz 1997; Bouillon et al. 2009). This method adds an artificial time scale term to control the rate of damping of elastic waves for regularization.

2.2 Configuration of the numerical models

The ocean starts from rest with the temperature and salinity fields initialized from the World Ocean Atlas 2013 (WOA13) climatology (Locarnini et al. 2013; Zweng et al. 2013). Grid cells are initialized with sea ice when the sea surface temperature (SST) is less than 2°C above the freezing point of seawater. We prescribe river runoffs with the climatological dataset of Dai and Trenberth (2002) north of 60°S. In the south of this latitude, the product of Merino et al. (2016) prescribes the freshwater flux due to melting icebergs. The model distributes the ice shelf calving fluxes along the calving front, following Depoorter et al. (2013). NEMO-LIM3 uses a sea surface salinity (SSS) restoring towards the WOA13 climatology to avoid spurious model drifts. Its relaxation is reduced proportionally to the ice concentration to preserve ocean–ice interactions in polar regions. The relaxation time scale is equivalent to 300 days for a mixed layer depth of 50m in the absence of sea ice.

The ocean and sea ice models share the same 1° curvilinear tripolar horizontal ORCA grid (Madec and Imbard 1996). This horizontal grid has a cell edge length of ∼112km at the equator, down to ∼46km in the Arctic Ocean. There are 75 levels along the vertical axis in partial step z-coordinates. The vertical resolution ranges from 1m near the ocean surface to 200m near the ocean floor, following a double hyperbolic tangent function.

The surface boundary conditions of NEMO-LIM3 are computed using the formulation of the Coordinated Ocean-ice Reference Experiments (CORE-II) of NEMO-LIM3. We select the DRAKKAR forcing set (DFS), version 5.2 (Brodeau et al. 2010; Dussin et al. 2016) to prescribe the atmospheric surface state. This atmospheric dataset, which covers the period 1958–2015, extends the ERA-interim reanalysis (Dee et al. 2011) prior to 1979 using the ERA40 product (Uppala et al. 2005) and a set of corrections (Dussin et al. 2016). DFS provides NEMO-LIM3 with the wind velocity components at 10m, the specific humidity and air temperature at 2m, the solid and liquid precipitation rates, and the shortwave and longwave radiations.

2.3 Landfast ice process parameterizations

2.3.1 Sea ice tensile strength scheme

Our implementation of the sea ice tensile strength in LIM3 is identical to the ones of Huot (2021) and Van Achter et al. (2022). This implementation is based on the initial work by König Beatty and Holland (2010) and the later studies by Itkin et al. (2015) and Lemieux et al. (2016). We adjust the isotropic tensile strength (T) using the parameter $k_t = T/P_p$, where P_p is the compressive sea ice strength (Lipscomb et al. 2007) . $k_t = 0$ is equivalent to no tensile strength ($T = 0$). $k_t = 1$ gives as much tensile strength as compressive strength ($T = P_p$).

The constitutive law relates the components of the internal ice stress tensor, σ_{11}, σ_{12} and σ_{22}, to the components of the strain rate tensor: the horizontal divergence $D_D = \partial u/\partial x + \partial v/\partial y$, tension $D_T = \partial u/\partial x - \partial v/\partial y$ and shear $D_S = \partial u/\partial y + \partial v/\partial x$ strain rates, where u and v are the horizontal ice velocity vector components. Let us define e as the eccentricity of the elliptical yield curve (ellipse ratio) for sea ice, Δ a measure of the deformation rate given by $\sqrt{D_D^2 + (D_T^2 + D_S^2)/e^2}$, $\sigma_1 = \sigma_{11} + \sigma_{22}$ and $\sigma_2 = \sigma_{11} - \sigma_{22}$. The internal stresses are determined by:

$$\frac{\partial \sigma_1}{\partial t} + \frac{\sigma_1}{2T_d} + \frac{p}{2T_d} = \frac{\zeta}{T_d} D_D \tag{1}$$

$$\frac{\partial \sigma_2}{\partial t} + \frac{e^2 \sigma_2}{2T_d} = \frac{\zeta}{T_d} D_T \tag{2}$$

$$\frac{\partial \sigma_{12}}{\partial t} + \frac{e^2 \sigma_{12}}{2T_d} = \frac{\zeta}{2T_d} D_S \tag{3}$$

where ζ is the bulk viscous coefficient, p is a pressure like-term, and T_d corresponds to the elastic damping timescale. Following König Beatty and Holland (2010), $\zeta = P_p(1 + k_t)/(2\Delta)$ and $p = (1 - k_t)P$. P is a replacement pressure term for P_p to ensure that p tends to zero when the deformation rate is near zero. Further, Δ is imposed a minimum value to avoid divisions by zero.

In sea ice models, the resistance of sea ice to tension has customarily been defined as null at a large scale, assuming that the number of ice leads is large in 100km elements (Coon 1980). However, observational evidence has shown that this assumption is not valid for sea ice on scales from 10 to 100km (Coon et al. 2007) and landfast ice (Tremblay and Hakakian 2006; König Beatty 2007). The tensile strength is often given as 1/20th of the compressive strength ($k_t = 0.05$) (e.g., Hibler and Schulson 2000; Wang 2007; Lemieux et al. 2018). Tremblay and Hakakian (2006) suggest a range of values for k_t between 0.5 and 0.8 based on reanalyses and satellite observations.

Setting $e = 2$ is usual in most sea ice models based on a viscous-plastic ice rheology (Bouchat et al. 2022; Hutter et al. 2022). This value is standard for e in LIM3. Yet, observations poorly constrain this parameter. Models studies exhibit better representations of landfast ice and reduced ice thickness biases for $e < 2$ (Miller et al. 2005; Dumont et al. 2009; Lemieux et al. 2016). Furthermore, Bouchat and Tremblay (2017) found a better agreement between the simulated and observed PDFs of the ice deformation rates when using $e < 2$.

As a result of these uncertainties, model studies examining landfast ice select various values for k_t and e. Itkin et al. (2015) used $k_t = 0.5$ and $e = 2$ for modelling landfast ice where the water depth is less than 25m. Later, Lemieux et al. (2016) estimated ranges for these parameters as $0.1 < k_t < 0.2$ and $1.4 < e < 1.6$ based on sensitivity studies. Huot (2021) and Van Achter et al. (2022) modelled Antarctic landfast ice by prescribing icebergs and setting $k_t = 0.2$ and $1.2 < e < 1.4$. In this study, we select $k_t = 0.05$ and $e = 1.4$ for the sea ice tensile strength scheme following the updated work of Lemieux et al. (2018) and the studies of Coon et al. (1998) and Bouchat and Tremblay (2017). For the ice rheology formulation with no isotropic tensile strength, we use $k_t = 0$ and $e = 2$.

Figure 2 shows four different elliptical yield curves normalised by the compressive ice strength in principal stress space $(\sigma_{p,1}, \sigma_{p,2})$. The principal stress components $\sigma_{p,1}$ and $\sigma_{p,2}$ of the internal ice stress tensor correspond to the maximum and minimum normal stresses, respectively. They are obtained for the orientation of the system of coordinates with no shear stress: $\sigma_{p,1}, \sigma_{p,2} = \frac{\sigma_1}{2} \pm \sqrt{\left(\frac{\sigma_2}{2}\right)^2 + \sigma_{12}^2}$. Among these four yield curves, only those with $k_t > 0$ enter the first quadrant, enabling both $\sigma_{p,1}$ and $\sigma_{p,2}$ to be positive. In other words, yield curves with $k_t > 0$ allow sea ice to have isotropic tensile strength. Decreasing e results in greater uniaxial tensile strength, i.e., $\sigma_{p,2}$ enters the second quadrant and $\sigma_{p,1}$ enters the fourth quadrant. The combined effect of lowering e and setting $k_t > 0$ leads to higher resistance to pulling forces than the single effects of decreasing e or setting

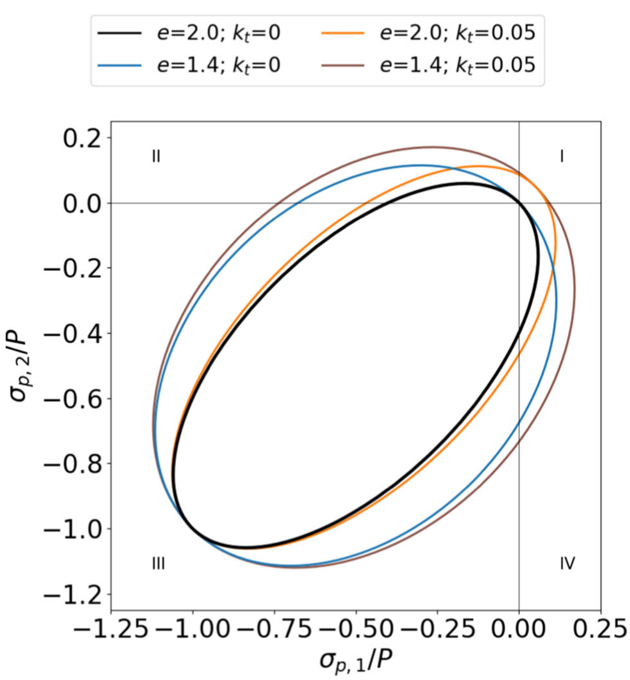

Fig. 2 Elliptical yield curves for sea ice normalised by the compressive ice strength (P) in principal stress space $(\sigma_{p,1}, \sigma_{p,2})$ with parameters $e = 2$ and $k_t = 0$ (continuous black), $e = 2$ and $k_t = 0.05$ (green), $e = 1.4$ and $k_t = 0$ (orange), $e = 1.4$ and $k_t = 0.05$ (dashed black)

$k_t > 0$. Indeed, the yield curve with $e = 1.4$ and $k_t = 0.05$ (black dashed ellipse) enclose the other yield curves shown in Fig. 2. Finally, the standard yield curve with $e = 2$ and $k_t = 0$ has little uniaxial tensile strength and no isotropic tensile strength.

2.3.2 Seabed stress scheme

The seabed stress scheme of Lemieux et al. (2015) represents the effect of grounded ice ridges on the seafloor. This scheme defines an additional seabed stress term $\vec{\tau_b}$ for the ice momentum equation. It relies on two free parameters: k_1 is a critical thickness parameter without units determining whether ice keels reach the seafloor; k_2 is a maximum seabed stress parameter (N/m^3) setting the magnitude of $\vec{\tau_b}$. The scheme considers ice ridges grounded if the mean ice thickness per unit area (h) is higher than the critical value $h_c = Ah_w/k_1$, where h_w is the water depth and A is the sea ice concentration. The seabed stress is calculated as follows:

$$\vec{\tau_b} = \begin{cases} k_2 \left(\frac{\vec{u}}{\|\vec{u}\|+u_o}\right)(h - h_c)\exp\left(-C_b(1-A)\right) & \text{if } h > h_c \\ 0 & \text{if } h \leq h_c \end{cases} \quad (4)$$

where $\vec{u}$ is the ice velocity, $u_0 = 5.0e - 5m/s$ is a small velocity parameter and C_b is a constant set here to 20. The factor in Eq. 4 on the right-hand side of k_2 ensures a smooth transition between static and kinetic friction regimes. $(h - h_c)$ represents the weight of the ice ridge above the hydrostatic balance. The exponential aims to decrease the seabed stress with the sea ice concentration.

In our current setup, the minimum ocean depth is 20m to ensure the numerical stability of the model in shallow water areas. However, this precludes the possibility of ice grounding in shallow waters. To circumvent this limitation, we implemented in NEMO-LIM3 a specific non-truncated bathymetry file providing h_w to the seabed stress scheme. We kept the minimum ocean depth as 20m in the ocean model. This approach allows for refined coastal bathymetry for the seabed stress scheme and a preserved ocean model stability in shallow water areas. We interpolated the ETOPO1 - 1 Arc-Minute Global Relief Model (Amante 2009) onto the horizontal grid of the model to create this specific bathymetry for the seabed stress scheme.

The simulated landfast ice is highly sensitive to k_1 but only moderately sensitive to k_2 (Lemieux et al. 2015). For this reason, we selected k_2=15N/m^3, as suggested by Lemieux et al. (2015). We estimated the best value of k_1 for our model setup by building a cost function with k_1 as the unknown variable. This cost function calculates the root mean square error of the total landfast ice area in shallow waters (depth less than 30m) between any two datasets. We minimised this cost function over 2006–2015 using the extension of the National

Ice Center (NIC) observations provided by Environment and Climate Change Canada (ECCC) (Dupont et al. 2022) and a simulation including the tensile strength scheme with no seabed stress scheme. The minimum of this cost function is $k_1 = 7.8$. We rounded k_1 to 8 in this study to agree with Lemieux et al. (2015).

2.4 Experimental setup

We performed four model runs with a global configuration of NEMO-LIM3 from 1958 to 2015. The analysis is restricted to the last 35 years to exclude spin-up effects. The number of sub-iterations for the EVP algorithm is increased to 920 in the four model runs to allow convergence of this algorithm (Lemieux et al. 2016). The first experiment is a control run (CTRL). This run uses no specific landfast ice process schemes. In the SEABED run, the seabed stress scheme (Lemieux et al. 2015) is activated. In the TENSILE run, we select the tensile strength (König Beatty and Holland 2010). Finally, we use the two landfast ice process schemes simultaneously in the fourth run (TENSEAB). Table 1 summarises the settings of the landfast ice process schemes utilised in these four model runs:

2.5 Diagnostics assessing the stability of the Arctic halocline

We define the depth of the upper boundary of the Arctic halocline as the surface mixed layer depth (H_{SML}), following Polyakov et al. (2018). We chose the definition of NEMO-LIM3 for calculating this depth. It corresponds to the depth at which the density is 0.01kg/m^3 higher than the density at 10m depth. This definition likely overestimates the simulated mixed layer depth in deep convection regions (Courtois et al. 2017) but is found appropriate for polar regions (Barthélemy et al. 2015; Peralta-Ferriz and Woodgate 2015).

The depth H_{halo} of the base of the Arctic halocline is calculated following Bourgain and Gascard (2011) by using the density ratio:

$$R_\rho = \alpha \frac{\partial\theta/\partial z}{\beta\partial S/\partial z} \tag{5}$$

where α is the seawater thermal expansion coefficient, β is the seawater haline contraction coefficient, θ is the potential temperature and S is the salinity. R_ρ evaluates the relative importance of the thermal and haline contributions to the stratification of the ocean. A large (small) R_ρ corresponds to a stratification dominated by temperature (salinity). According to Bourgain and Gascard (2011), the depth at which R_ρ is equal to 0.05 marks the transition between the Arctic halocline and the Atlantic water of the Arctic Ocean. This depth corresponds to H_{halo}.

The available potential energy (APE) is the amount of the total potential energy available for conversion into kinetic energy via adiabatic redistribution of the density field (Lorenz 1955). This energy can be converted to kinetic energy, for example, through baroclinic instabilities. Contrary to the Brunt-Väisälä buoyancy frequency, the APE provides an overall bulk measure of the stability of the stratification of an ocean layer. We calculate the APE by integrating potential density anomalies vertically from the surface down to the base of the halocline layer, as suggested by Polyakov et al. (2018):

$$APE = \int_0^{H_{halo}} g\left(\rho - \rho_{ref}\right) z dz \tag{6}$$

where z is the vertical depth with $z = 0$ referenced by the sea surface, g is the acceleration due to gravity, ρ and ρ_{ref} are the potential density at z and H_{halo}, respectively. The term $\int_0^{H_{halo}} g\rho_{ref} z dz$ corresponds to the reference potential energy of a homogeneous density profile. APE diagnoses how much potential energy deviates from this homogeneous density profile. Thus, the APE reflects the strength of the ocean stratification. The greater the APE, the stronger the ocean stratification.

Table 1 Names and descriptions of the simulations carried out in the study

	CTRL	SEABED	TENSILE	TENSEAB
k_1	0	8	0	8
k_2	0	15	0	15
k_t	0	0	0.05	0.05
e	2	2	1.4	1.4

k_1 is a critical thickness parameter without units, k_2 is the maximum seabed stress parameter (N/m^3), k_t is the isotropic tensile strength fraction, and e is the ellipse ratio of the ice yield curve

3 Results and discussion

3.1 Validation of the numerical simulations

3.1.1 Validation of Arctic landfast ice

In this section, we assess the simulation of the Arctic landfast ice cover by NEMO-LIM3 using the National Ice Center (NIC) sea ice charts in gridded format (Fetterer and Fowler 2006) from 1980 to 2007 and an extension of this product made by the Environment and Climate Change Canada (ECCC) from 2008 to 2015 (Dupont et al. 2022). NIC sea ice charts are analyses performed by experts of available in-situ, remote sensing, and model data weekly or bi-weekly (Dedrick et al. 2001). These charts suffer from discontinuities linked to the increasing number of data sources available to the analyst, the level of expertise of the latter, changes in procedures and conventions and errors due to data transformations and re-gridding. Furthermore, more attention to details has been paid to areas of high interest for the NIC (e.g., the Beaufort, Chukchi and Bering Seas) compared to some other regions (e.g., the Central Arctic) (Fetterer and Fowler 2006). Figure 3 displays the map of the frequencies of landfast ice occurrences based on the NIC observational datasets of Fetterer and Fowler (2006) and Dupont et al. (2022). In NEMO-LIM3, we define sea ice as landfast ice when the two-week average sea ice speed is less than 5mm/s, following Van Achter et al. (2022). The discrepancy between the model and NIC definitions of landfast ice arises from the difference in methodology between the modelled sea ice velocities and interpreted sea ice charts.

In addition to the landfast ice occurrence frequencies, we examine the mean seasonal cycles of the observed and modelled landfast ice extents in the Arctic Ocean and its peripheral seas (Fig. 5). The landfast ice extent from the NIC sea ice charts corresponds to the total grid cell area marked as landfast ice within a defined spatial domain. In NEMO-LIM3, the landfast ice extent is the total grid cell area covered by landfast ice in a spatial domain and where the ice concentration is at least 15%. This sea ice concentration threshold

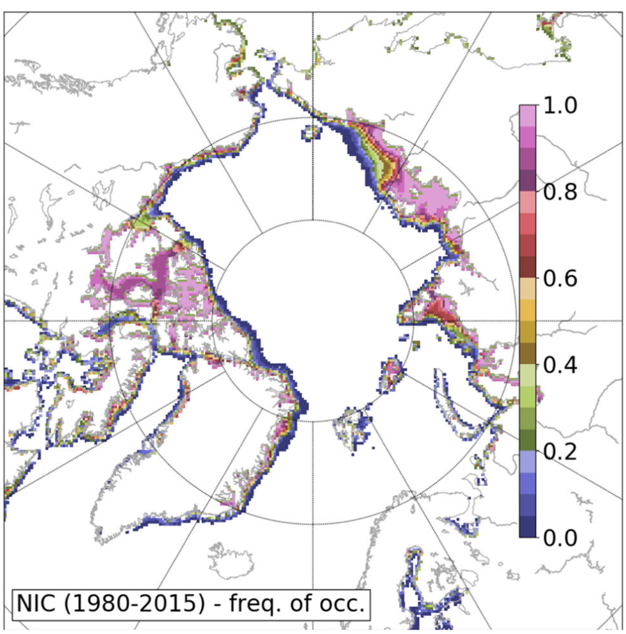

Fig. 3 Frequency of occurrence of landfast ice for January to June from datasets based on the National Ice Center (NIC) sea ice charts (Fetterer and Fowler (2006) for 1980-2007 and Dupont et al. (2022) for 2006-2015)

reflects the commonly admitted method for calculating the sea ice extent.

The spatial distribution of the frequency of occurrence of landfast ice from the TENSEAB run (Fig. 4d) is in relatively good agreement with the NIC observations (Fig. 3). Additionally, the seasonality of the total Arctic landfast ice extent from the TENSEAB run compares well with the NIC datasets (Fig. 5f). Most of the modelled landfast ice in the TENSEAB run is located in the CAA (Figs. 4d and 5d). Landfast ice in this region is due to the interlocking of sea ice between islands and narrow channels (Lemieux et al. 2018). The TENSEAB run overestimates the landfast ice extent in the CAA all year round. This overestimation could be due to the missing effect of tides on the landfast ice cover in our model setup. Indeed, The modelling study of Lemieux et al. (2018) shows that tidal effects enhance the ice–ocean stress, which leads to a decrease in the landfast ice area in some regions of the CAA.

In winter, the total landfast ice extent simulated in the CTRL run in the Arctic Basin is approximately half the value of the landfast ice extent observed from the NIC sea ice charts and simulated in the TENSEAB run (Fig. 5). This underestimation is one argument supporting the inclusion of landfast ice process schemes to simulate Arctic landfast ice. However, the results from the CTRL run suggest that the default setting of the elliptical yield curve in LIM3 is sufficient to resolve landfast ice in the CAA. Indeed, this model run exhibits a high frequency of occurrence of landfast ice in the CAA from January to June (Fig. 4a). This feature agrees with the NIC observations (Fig. 3) and compares well with the outputs from the other model runs (Fig. 4b–d). Landfast ice is sustainable in the CAA without isotropic sea ice tensile strength thanks to the uniaxial tensile strength property of the elliptical yield curve (Olason 2016). Note that this is possible only if the EVP algorithm fully converges.

In the Beaufort and Chukchi Seas, the observed landfast ice appears as a narrow strip of sea ice attached to the coastline (Mahoney et al. 2007; Yu et al. 2014). In these two seas, easterly prevailing winds and ocean surface currents yield highly deformed ice ridges and rubble piles known as stamukhi that become grounded in winter (Reimnitz et al. 1994). The mid-season landfast ice edge in the Beaufort Sea resides near the 18m isobath (Mahoney et al. 2007). The horizontal model resolution does not allow a good representation of this narrow landfast ice strip (Fig. 4d). Instead, the TENSEAB run features pixel-sized points with high frequencies of landfast ice occurrence along the coastline.

The grounding of ice ridges is the principal mechanism for sustaining landfast ice over large distances to the shore in the LESS (Haas et al. 2005; Selyuzhenok et al. 2015; Lemieux et al. 2016; Selyuzhenok et al. 2017; Liu et al. 2022). For this reason, the seabed stress scheme is skillful in allowing for the emergence of landfast ice in the LESS (Fig. 4b). In these regions, the CTRL run presents some occurrences

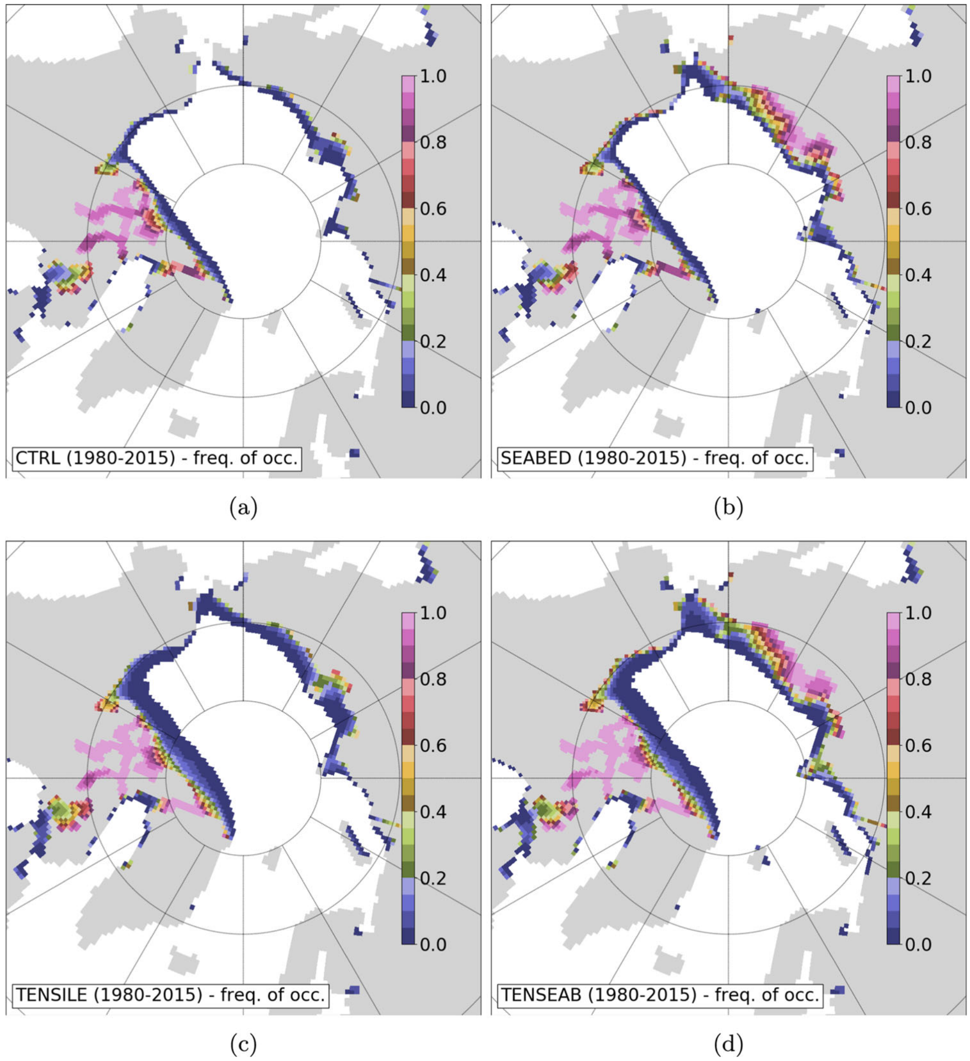

Fig. 4 Frequency of occurrence of landfast ice (1980–2015) for January to June from the CTRL (a), SEABED (b), TENSILE (c) and TENSEAB (d) runs

of landfast ice close to the shoreline. Moreover, the TENSILE run exhibits static ice arches between the New Siberian Islands (145°E) and Siberia. However, only the simulations with the seabed stress parameterization achieve a spatial distribution of landfast ice occurrence comparable to the one derived from the NIC products in these regions (Fig. 4b and d). Combining the tensile strength scheme with the seabed stress scheme improves the winter maximum in landfast ice extent in the Beaufort and Laptev Seas (Fig. 5e and b). The increased tensile strength allows a longer offshore extension of landfast ice, thanks to using grounded ice ridges as fastening platforms. In the East Siberian Sea, the maximum winter landfast ice extent from the TENSEAB and SEABED runs are nearly identical (Fig. 5c), suggesting only a minor role of the sea ice tensile strength in the landfast ice development in this region.

According to Divine et al. (2005), the landfast ice in the Eastern Kara Sea follows three principal spatial configurations (modes). The bathymetry and a chain of islands constrain these spatial modes. The so-called S-mode, the most frequent of these three modes, is visible in Fig. 3 between Severnaya Zemlya (around 97°E) and the coast of Siberia. This spatial mode is seen in Fig. 3 as the ice arch where the frequency of landfast ice occurrence is more than 0.60 in the Kara Sea, westward of Severnaya Zemlya. Neither the TENSILE nor the SEABED run displays an S-mode comparable to the one seen in the NIC observations. The two landfast ice process schemes must be combined to model this spatial mode in the Laptev Sea (Fig. 4d). In the Kara Sea, the TENSEAB run underestimates the frequency of occurrence of landfast ice by ∼0.40 (Fig. 4d) and the observed winter maximum in landfast ice extent by a factor of two (Fig. 5a). These underestimations may appear disappointing regarding the past modelling studies of Olason (2016) and Lemieux et al. (2016). In the study of Lemieux et al. (2016), the numerical simulation prescribing $e = 1.4$, $k_t = 0$ and no seabed stress is the closest to our SEABED run in terms of the landfast ice parameters. This simulation from Lemieux

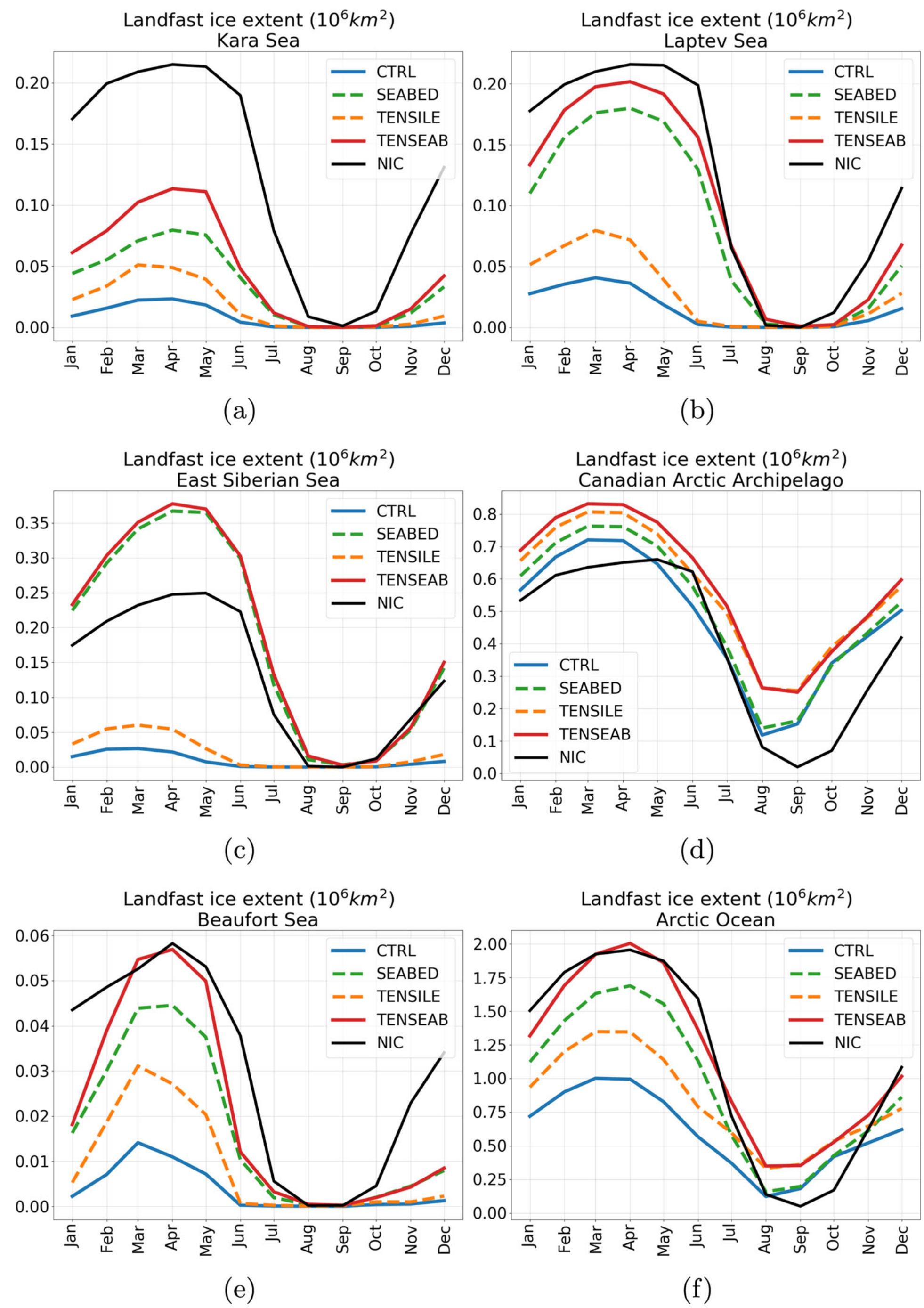

Fig. 5 Mean seasonal cycles of the landfast ice extent (1980–2015) in the Kara Sea (a), Laptev Sea (b), East Siberian Sea (c), Canadian Arctic Archipelago (d), Beaufort Sea (e) and Arctic Ocean (f). The black line corresponds to the NIC observational dataset (Fetterer and Fowler 2006) extended by the ECCC dataset (Dupont et al. 2022). The blue, orange, green and red lines correspond to the CTRL, SEABED, TENSILE and TENSEAB runs, respectively. Figure 1 shows the spatial domain used to integrate the landfast ice extent

et al. (2016) tends to overestimate the seasonal maximum in landfast ice extent in the Kara Sea, whereas our SEABED run underestimates this seasonal maximum (Fig. 5a). Thus, the tuning of sea ice tensile strength in our study is unlikely to have caused the underestimation of the modelled landfast ice extent in the Kara Sea. On the other hand, our 1° horizontal model resolution is coarser than the horizontal grids used by Lemieux et al. (2016) and Olason (2016). Liu et al. (2022) improved the simulation of landfast ice in their model setup by replacing the lateral boundary condition with a coastal drag term to represent subgrid interactions with small islands and bathymetric features. These highlight that the sea ice tensile strength and seabed stress are not the only factors controlling the landfast ice development in the Kara Sea.

3.1.2 Validation of the Arctic sea ice characteristics

To evaluate the modelled Arctic sea ice concentration and velocity over 1980–2015, we select the Nimbus-7 SMMR and DMSP SSM/I-SSMIS passive microwave data products (Cavalieri et al. 1996) and the Polar Pathfinder sea ice motion vector dataset (Tschudi et al. 2019). We refer to these observations as NSIDC-SIC, and NSIDC-drift, respectively. Concerning the modelled sea ice thickness, we use the Pan-Arctic Ice Ocean Modeling and Assimilation System (PIOMAS) (Zhang and Rothrock 2003; Schweiger et al. 2011). Note that PIOMAS is not a pure observational product, but rather a reanalysis of sea ice based on a numerical ocean–sea ice model. This model system assimilates observed sea ice concentrations and sea surface temperatures to constrain the simulated sea ice state. With these three climate products, we evaluate the modelled mean seasonal cycles and time series in March and September of the total sea ice extent, total sea ice volume, and mean sea ice speeds in the Arctic. Orval (2021) analysed more extensively the simulated sea ice features from our four model runs. The interested reader may refer to the studies of Lecomte et al. (2015), Docquier et al. (2017), and Sterlin et al. (2021) for more insights on the simulation of Arctic sea ice using a similar model setup to ours.

The mean seasonal cycles of the total sea ice extent from the four model runs agree reasonably well with the NSIDC-SIC observations (Fig. 6a). However, the simulated minimum sea ice extent occurs about two to three weeks earlier than in the NSIDC-SIC products. This bias is common in other studies based on this model (Rousset et al. 2015; Lecomte et al. 2015; Docquier et al. 2017; Sterlin et al. 2021).

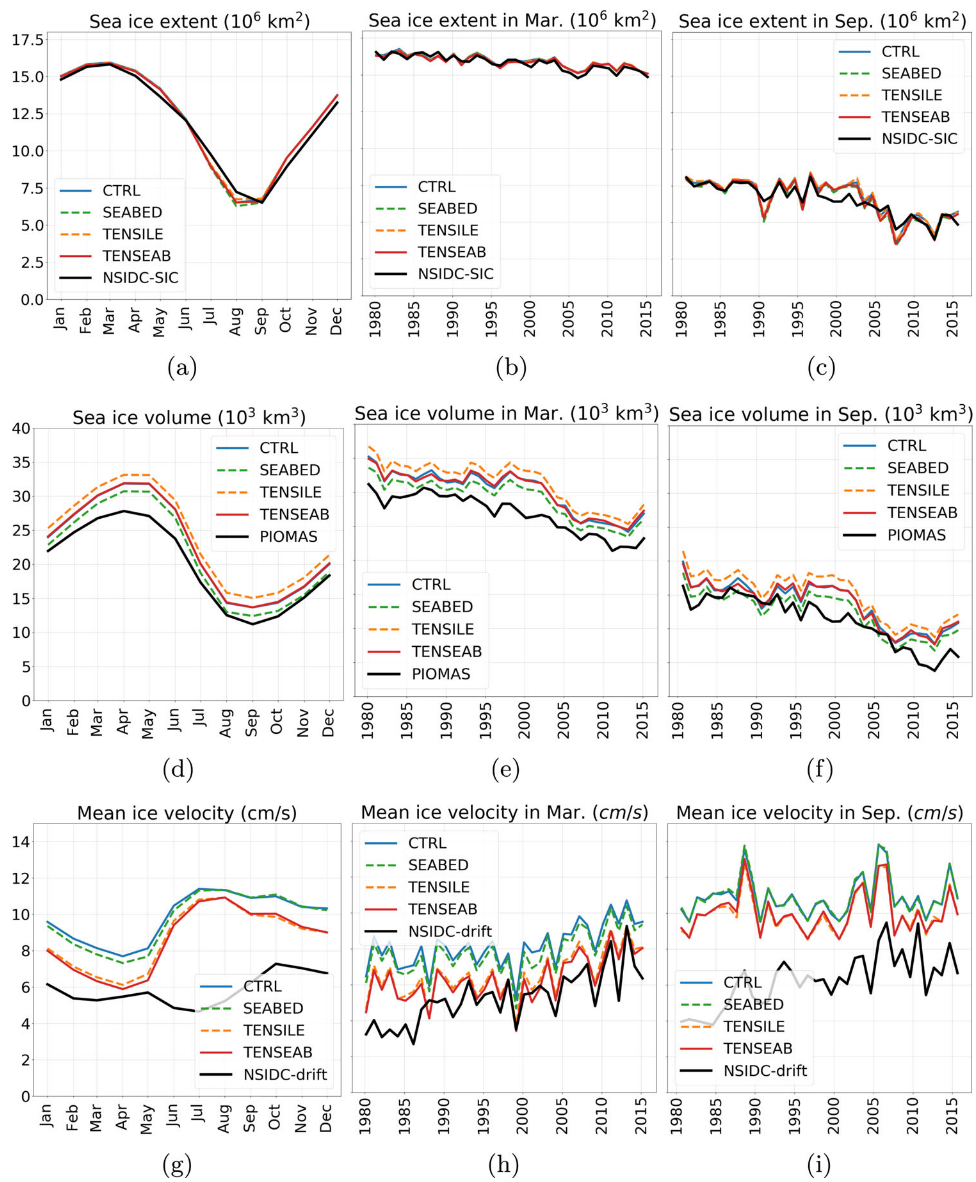

Fig. 6 Mean (1980–2015) seasonal cycles (left column) of the total sea ice extent (SIE) (a), total sea ice volume (SIV) (d) and mean sea ice speed (g). Times series in March (middle column) and September (right column) of the total SIE (b, c), total SIV (e, f) and mean sea ice speed (h, i). The mean sea ice speeds are calculated following the method of Tandon et al. (2018). The black dashed lines correspond to either the NSIDC-SIC (a–c), PIOMAS (d–f) or NSIDC-drift (g–i) datasets. The blue, orange, green and red continuous lines correspond to the CTRL, SEABED, TENSILE, and TENSEAB runs, respectively

NEMO-LIM3 accurately represents the decline in Arctic sea extent observed over the past decades in March (Fig. 6b) and September (Fig. 6c). This decline is more pronounced in September as observed (e.g., Fetterer and Fowler 2006). During this month, the trend in sea ice extent from the CTRL run amounts to -86860km^2 per year over 1980–2015, compared to -91772km^2 per year in the NSIDC-SIC observations.

The general shape of the mean seasonal cycle of the total sea ice volume from NEMO-LIM3 is similar to the one derived from PIOMAS (Fig. 6d). However, the total sea ice volumes from the model runs are overestimated by 0.8-3.4e3km^3 in October and 2.1–4.6e3km^3 in March compared to PIOMAS. On the other hand, the uncertainties in the total sea ice volume from the PIOMAS product are 1.35e3km^3 in October and 2.25e3km^3 in March (Schweiger et al. 2011). Thus, the total sea ice volume from NEMO-LIM3 is generally within the range of uncertainties of PIOMAS. NEMO-LIM3 and PIOMAS show a good agreement in terms of trend and variability in total sea ice volume for both March and September (Fig. 6e and f). The trend in sea ice volume from the CTRL run in September is -2.67e3km^3 per decade over 1980–2015, against -3.20 $\times\pm 1.0e$3km^3 from the PIOMAS reanalysis (Schweiger et al. 2011).

The mean sea ice speeds from NEMO-LIM3 and NSIDC-drift are calculated using the method of Tandon et al. (2018). This method aims to determine the mean sea ice drift of the Arctic ice pack. The spatial averaging domain excludes areas within 150km of the coast. The means are calculated from daily sea ice drift vector components to include sub-monthly variations in the ice drift direction (Docquier et al. 2017; Tandon et al. 2018).

In winter, the modelled mean sea ice speeds are close to the NSIDC-drift observations, especially for the simulations using the sea ice tensile strength scheme (Fig. 6g). In summer, the mean sea ice speeds increase in the four model runs as the sea ice pack tends to a free drift state. This behaviour is coherent with observations from the International Arctic Buoy Programme (IABP). Indeed, the observed sea ice speed from the IABP program is maximum in late summer when sea ice is thinner (Olason and Notz 2014). By contrast, NEMO-LIM3 simulates a seasonal maximum in mean sea ice speed in July–August. The timing of the seasonal maximum in sea ice speed in the simulations is consistent with the early seasonal minimum in sea ice extent simulated by NEMO-LIM3. The mean sea ice speed from the NSIDC-drift product does not display the observed late summer and early

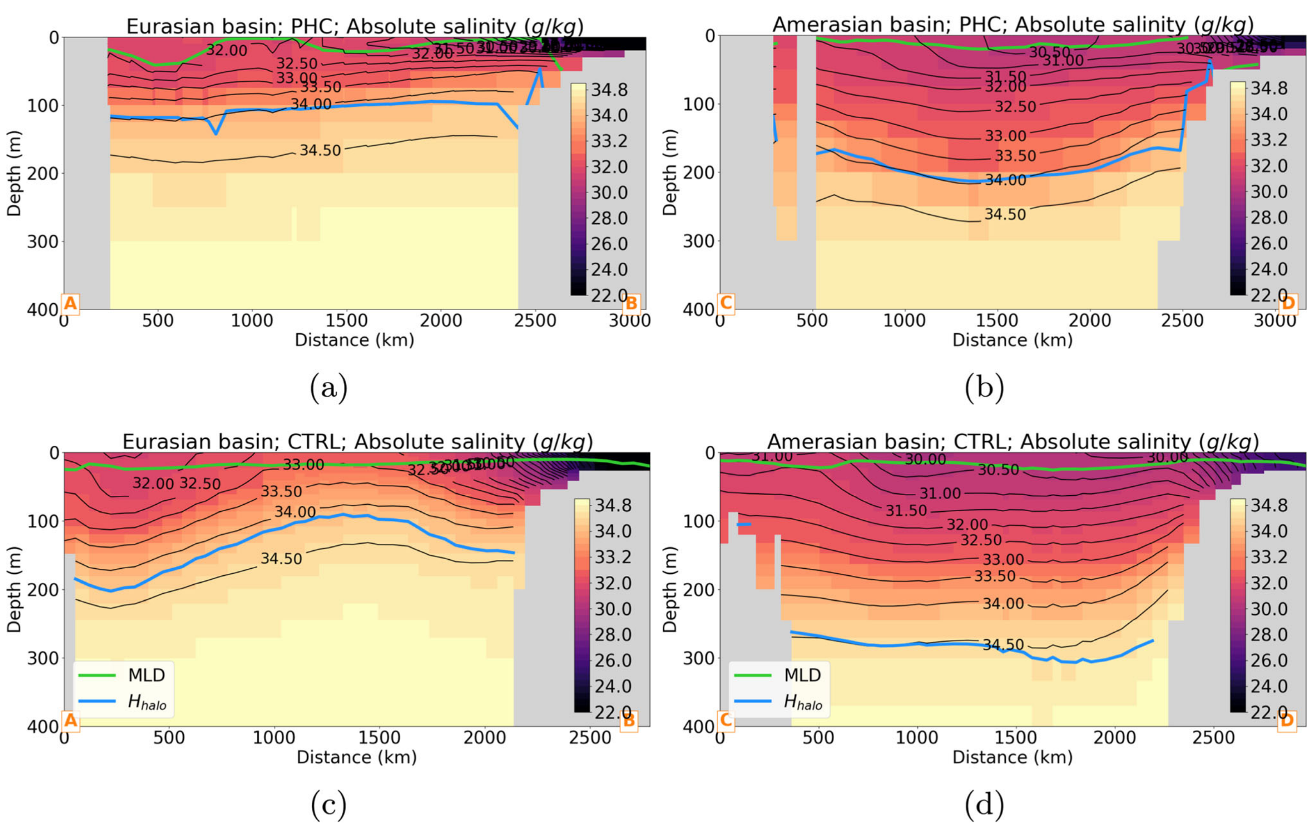

Fig. 7 Oceanic transects of salinity (g/kg) from the Polar Science Center Hydrographic Climatology (PHC), version 3.0 (a, b) and from the CTRL run (c, d) along the transects AB across the Eurasian Basin (a, c) and CD across the Amerasian Basin (b, d) (see Figure 1). The green and blue lines indicate the depth of the surface mixed layer (H_{SML}) and the lower boundary of the halocline layer (H_{halo}), respectively

winter seasonality from the IABP (Docquier et al. 2017). The NSIDC-drift dataset is prone to uncertainties, particularly during the melt season (Sumata et al. 2015; Szanyi et al. 2016). Lastly, the NSIDC-drift observations indicate positive trends in the mean sea ice speed in September and March. This increased mobility in the Arctic ice pack is confirmed by other studies (Rampal et al. 2009; Tandon et al. 2018; Lipatov et al. 2021) but is partially captured by our model configuration. The modelled trends (1980–2015) in Arctic sea ice drift in March are ~ 0.43cm/s per decade in our model simulations against 1.08cm/s in the NSIDC-drift observations. In September, these simulated trends are weak and not statistically significant. These contrast with the positive trend of 1.01cm/s seen in the NSIDC-drift observations. It is worth mentioning that the Climate Model Intercomparison Project Phase 5 (CMIP5) model experiments also fail to accurately represent the observed positive trends in Arctic mean sea ice speed (Rampal et al. 2009; Tandon et al. 2018). Moreover, the NSIDC-drift product is likely overestimating the trends in Arctic sea ice drift as these trends exceed the ones calculated by Tandon et al. (2018) using the IABP buoy measurements over a similar time span.

3.1.3 Validation of the structure and stability of the Arctic halocline

The Polar Science Center Hydrographic Climatology (PHC), version 3.0 (Steele et al. 2001) is selected to validate the structure and stability of the Arctic halocline simulated in the CTRL run. The CTRL run is chosen as a reference to exclude the effects of the landfast ice process parameterizations on the Arctic Ocean. We analyze two oceanic transects of salinity (Fig. 7) and potential temperature from the PHC and CTRL run (Fig. 8). The first transect AB runs across the Eurasian Basin and the second transect CD runs across the Amerasian Basin. The positions of these transects are shown in the bathymetry map (Fig. 1). Lastly, we examine the spatial distribution of the APE from the CTRL run in the Arctic regions (Fig. 9).

The Arctic surface mixed layer is a quasi-homogeneous layer that caps the Arctic Ocean. The melting and freezing cycles of sea ice, ocean surface stress, and heat fluxes control the thickness of this layer. The depth H_{SML} of the surface mixed layer is 20-30m in summer, down to 25-50m in the Western Arctic and 70–100m in the Eastern Arctic in winter (Peralta-Ferriz and Woodgate 2015). As mentioned in

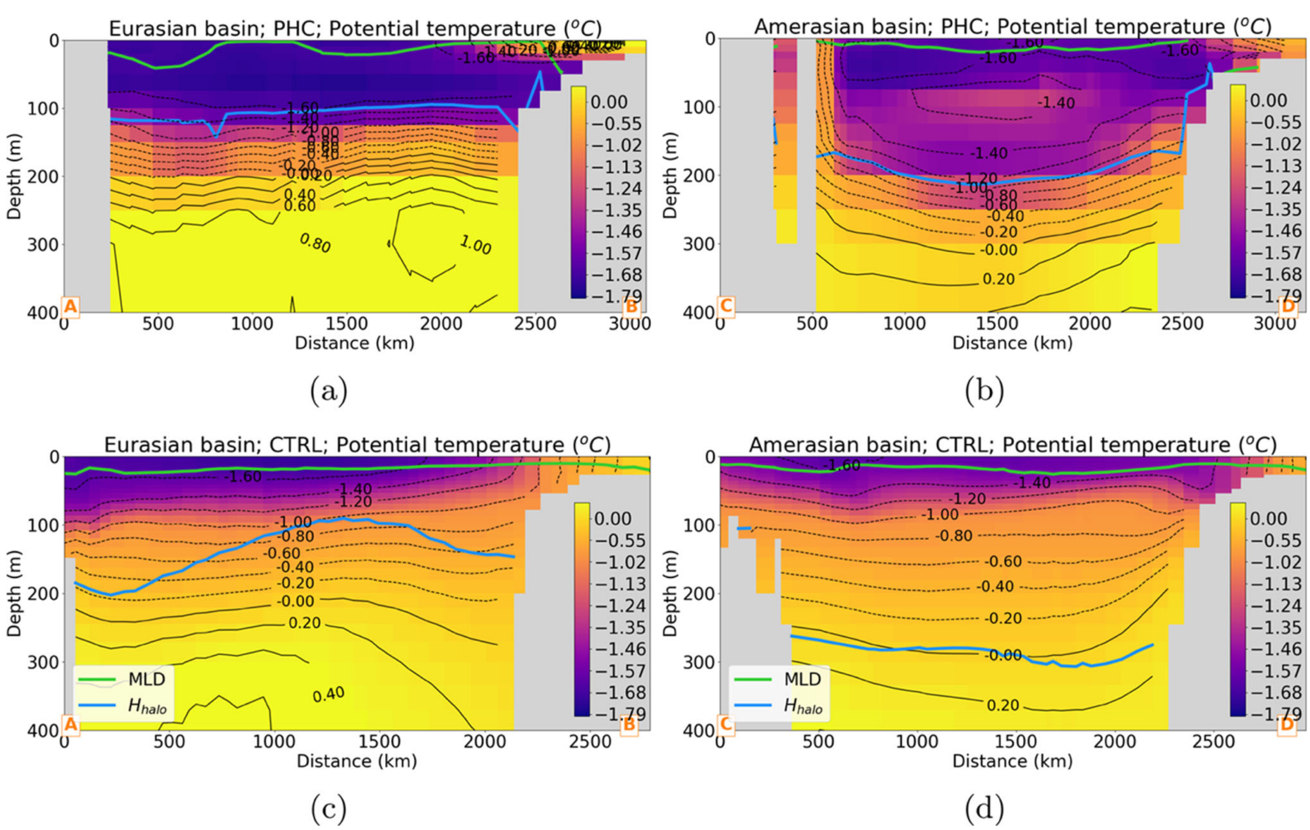

Fig. 8 Same as in Fig. 7, but for the potential temperature ($°C$)

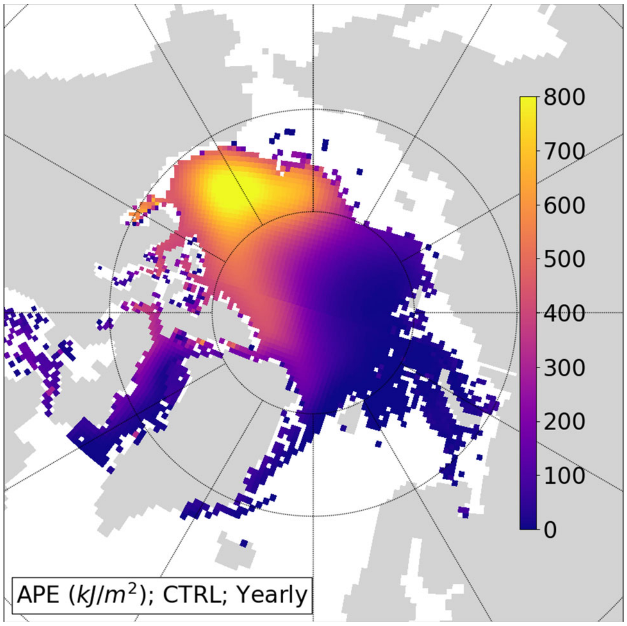

Fig. 9 Annual mean (1980–2015) available potential energy (APE) (kJ/m^2) integrated from the surface down to H_{halo} from the CTRL run. The APE is calculated for latitudes greater than 60° N where sea ice concentration is at least 15%

Section 2.5, H_{SML} forms the upper boundary of the Arctic halocline layer.

The Arctic halocline includes the upper halocline, also known as the cold halocline, and the lower halocline or permanent halocline. The upper and lower halocline layers sit below the surface mixed layer. This upper halocline layer is characterised by quasi-homogeneous near-freezing temperatures down to 50-100m (Polyakov et al. 2018). This layer is evident in the temperature transects from the PHC climatology (Fig. 8a and b). In the lower halocline, the salinity dominates the stratification. The transition from salinity to temperature-driven stratification regimes marks the base of the halocline (Bourgain and Gascard 2011; Polyakov et al. 2018). The base of the lower halocline layer lies at a depth between 100-150m and $\sim$ 200m in the Eurasian and Amerasian Basins, respectively (Timmermans and Marshall 2020).

The relatively warm and saline water mass below the Arctic halocline is characteristic of the Atlantic water of the Arctic Ocean. Atlantic waters flow into the Arctic Basin through the Fram Strait and the Barents Sea Opening. During their transits, the upper parts of these two branches undergo freshening and cooling, such that the warm core of the AW branches resides at depth (Timmermans and Marshall 2020). The Fram Strait and Barents Sea branches meet north of the Kara Sea (Dmitrenko et al. 2015). These two branches merge and circulate in the Arctic at intermediate depths along the continental slopes and ridges of the basin cyclonically (Rudels et al. 1994).

The oceanic transects from the PHC climatology exhibit the vertical structure of the Beaufort Gyre (Fig. 7b and b). The relatively warm temperature (more than −1.4 °C) below the upper halocline layer at 60-220 m depth is a signature of Pacific waters (Pickart et al. 2005; Carmack et al. 2016). Pacific waters flow into the Arctic Ocean via the Bering Strait and the Chukchi Sea. From there, these waters propagate into the Amerasian Basin (Steele et al. 2004). The direction of the Pacific outflow is dictated by wind conditions, and the strength and extent of the Beaufort Gyre (Lin et al. 2021). The Pacific water ventilates the upper halocline (Pickart 2004). Lastly, the transects across the Amerasian Basin show cold and hypersaline waters (salinity more than 34g/kg) sandwiched between the relatively warm Pacific and Atlantic waters. This hypersaline water mass originates from brine-enriched waters produced in the coastal polynyas located along the coast of Alaska (Weingartner et al. 1998). It then ventilates the lower halocline of the Amerasian Basin (Weingartner et al. 1998).

The salinity transects from the CTRL run do not fully agree with the PHC climatology (Fig. 7). The CTRL run overestimates the ocean salinity between the surface mixed layer and the upper halocline layer by about 1.0g/kg in the interior of the Eurasian Basin (Fig. 7a and c). On the other hand, this simulation underestimates the salinities towards Greenland and in the Laptev Sea by $\sim$ -0.6g/kg and $\sim$0.6g/kg, respectively. These underestimations are associated with the too steep isohaline contours simulated in these regions compared to the PHC climatology. In the Amerasian Basin, the salinities from the CTRL run are $\sim$ -0.4g/kg smaller than the PHC observations (Fig. 7b and d). These fresh salinity biases are related to too deep transitions between salinity and temperature-driven stratification regimes in the CTRL run compared to the PHC observations. Consequently, the CTRL run overestimates H_{halo} by 30-50 % with respect to the PHC climatology in the Eurasian Basin towards the Laptev Sea and Greenland, as well as in the Amerasian Basin.

The potential temperature transects from the CTRL run present noticeable differences compared to the PHC climatology (Fig. 8). Our configuration of NEMO-LIM3 poorly simulates the upper (cold) halocline layer. The near-freezing temperatures are confined to a shallow water region roughly corresponding to the surface mixed layer in the CTRL run. Below this region, the temperature increases with depth. The poor simulation of the cold halocline layer is a recurrent problem of ocean general circulation models. For instance, similar biases are present in the models that participated in the Arctic Ocean Model Intercomparison Project (AOMIP) (Holloway et al. 2007).

The transects in the Amerasian Basin from the CTRL run show no sign of warm Pacific waters and cold hypersaline waters, as observed by Weingartner et al. (1998). These absences are related to the modelled extent and strength of the Beaufort Gyre. Indeed, NEMO-LIM3 simulates a warm water mass analogue to Pacific water in the Beaufort Sea (not shown). However, we find no clue of a cold hypersaline water mass in the CTRL run. Note that the 1° horizontal grid of our model setup resolves Bering Strait using two points at the minimum width of this strait (83 km). Lastly, our model setup fails to simulate the observed horizontal stratification in the shallow Siberian shelves.

According to Ilıcak et al. (2016), there is a large spread in the simulated temperature of the Arctic Ocean between CORE-II forced ocean–sea ice models. These authors identified two processes contributing to the temperature spread: 1) the inflow of warm Atlantic water at Fram Strait and 2) the formation of cold and dense water on the eastern shelf. As the NEMO-based models reviewed by Ilıcak et al. (2016), our model presents a cold bias in the Atlantic water. This bias is more pronounced in the Eurasian Basin. Ilıcak et al. (2016) pointed to either an issue with the vertical mixing of the cold bias anomaly or simply a too weak advection of heat in the Eurasian Basin. CORE-II forced models show fresh ocean biases between 50 and 400m (Ilıcak et al. 2016). In the CTRL run, this negative salinity bias is clear in the Amerasian Basin (Fig. 7b and d). The underestimated salinity in the model in the upper Arctic Ocean is possibly due to the representation of brine rejection and vertical mixing in models (Nguyen et al. 2009; Ilıcak et al. 2016). Barthélemy et al. (2015) found that the brine rejection parameterization of Nguyen et al. (2009) acts to restratify the polar mixed layer in NEMO-LIM3, which is unrealistic. More complex brine rejection parameterizations with a dependence on the ice thickness distribution have shown mitigated results (Barthélemy 2016). More generally, analyses of the deep Arctic Ocean in Climate Model Intercomparison Project phase 6 (CMIP6) models suggest significant model biases related to the inaccurate representation of shelf processes (Heuzé et al. 2023).

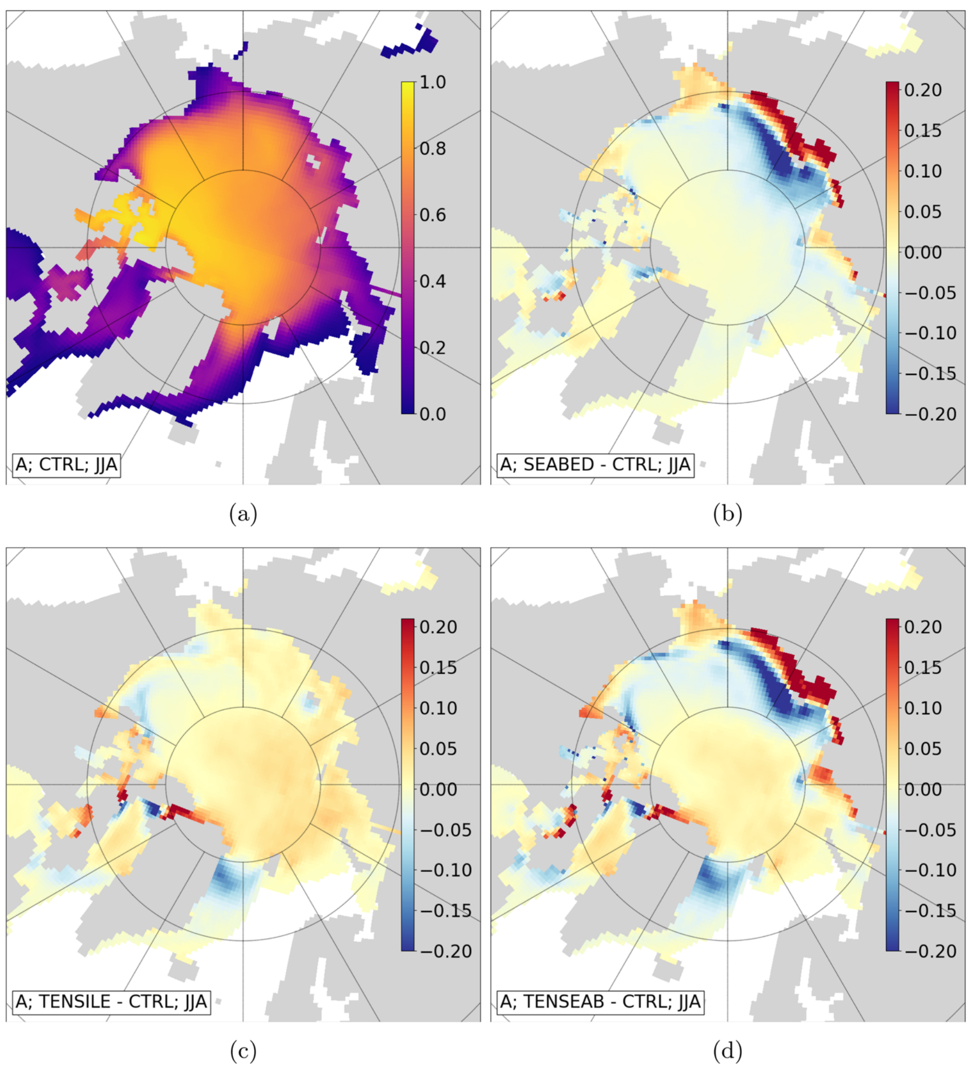

Fig. 10 June-July-August (JJA) mean (1980–2015) sea ice concentration (A) from the CTRL run (a), and sea ice concentration differences between the SEABED and CTRL runs (b), the TENSILE and CTRL runs (c), the TENSEAB and CTRL runs (d)

The spatial distribution of the APE from the CTRL run (Fig. 9) is close to the one shown by Polyakov et al. (2018). As expected, the APE is the largest in the Amerasian Basin, where the Beaufort Gyre allows freshwater storage and strong stratification. APE is small in the Eurasian Basin due to a weaker stratification of the halocline layer. Polyakov et al. (2018) estimated the APE in the Beaufort region as 120kJ/m^2 in the early 1980s and 300kJ/m^2 in the late 2010s using hydrographic data. Regan et al. (2020) calculated the APE in the Beaufort Gyre as 220 to 400kJ/m^2 from 1990 to 2015, using a high-resolution, eddy-resolving ocean model. We calculate an APE of 320kJ/m^2 in the Beaufort Gyre based on the PHC climatology. These values contrast with the ones from our CTRL run. The simulated annual mean (1980–2015) APE in the Beaufort Sea is ~800kJ/m^2 in the CTRL run. In the Amerasian Basin, the base of the simulated halocline layer lies at a deeper depth than in the PHC climatology. Therefore, the simulated density anomalies from the CTRL run are integrated over a longer vertical distance than in the PHC climatology. The simulated halocline layer in the Amerasian Basin is less dense because of a fresher ocean with respect to the PHC climatology. These lighter water parcels increase the simulated density anomalies ($\rho - \rho_{ref}$) and hence the APE in the Beaufort Gyre (Eq. 6). Potential temperature biases in the halocline layer are less relevant for explaining the density anomalies because of the low-density ratio ($R_\rho < 0.05$). Therefore, we expect only a minor effect of the poor representation of the cold halocline layer on the simulated APE.

3.2 Arctic sea ice sensitivity to the landfast ice process schemes

3.2.1 Impact of the seabed stress scheme on sea ice conditions

The seabed stress scheme impacts the spatial distribution of sea ice concentration in the LESS in June-July-August (JJA)

Fig. 11 Same as in Fig. 10, but for the annual mean sea ice thickness (h) (m)

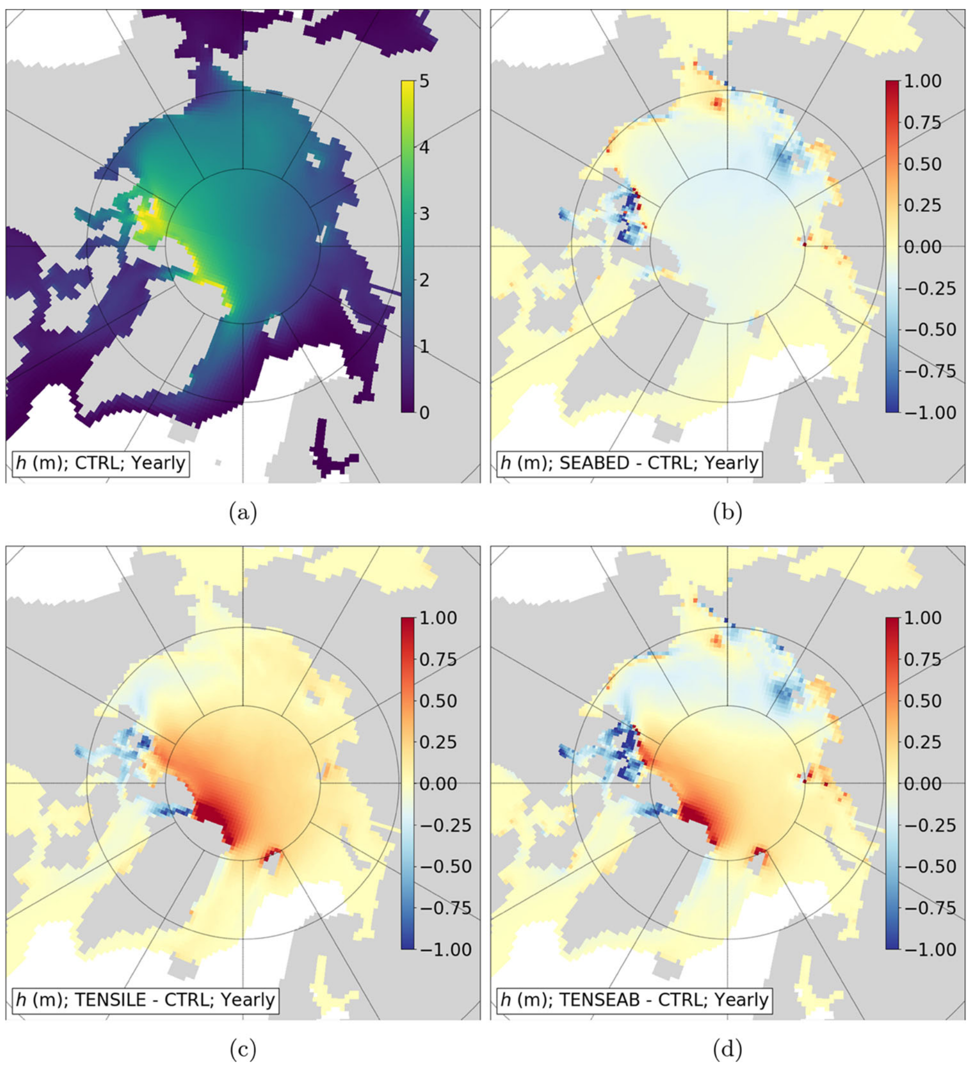

(Fig. 10b). During this period, the simulated sea ice concentration from the SEABED run is higher towards the coast but smaller offshore at the Siberian shelf break compared to the CTRL run. In winter, the ice concentrations from the SEABED and CTRL runs are close to unity, with only minor differences between these two simulations.

The landfast ice edge marks the boundary between landfast ice and drift ice. In the coastal regions of Siberia, flaw polynyas develop in this boundary due to prevailing winds blowing offshore (Reimnitz et al. 1994). During the melt season, the flaw polynyas turn into hotspots for high ocean heat gain in the open water fraction, promoting sea ice losses (Reimnitz et al. 1994; Morales Maqueda et al. 2004). With the seabed stress scheme, the fresh and cold shelf waters below the landfast ice cover delay the melting of sea ice in coastal regions during the melt season, as we will see in Section 3.3.

When the seabed stress scheme is activated, the annual mean sea ice thickness (Fig. 11b) is generally smaller where the frequency of occurrence of landfast ice is high (Fig. 4b), especially in the CAA and the LESS. In the Eurasian Basin, the simulated ice thickness is ∼20cm smaller when using the seabed stress scheme. However, this scheme leads to positive local differences in sea ice thickness (up to 40 cm) in the vicinity of the coast or small islands. Lemieux et al. (2015) and Itkin et al. (2015) reported similar spatial differences in the simulated ice thickness when improving the representation of landfast ice in their model setup.

To investigate the origin of the differences in sea thickness between the SEABED and CTRL runs, Fig. 12 displays the map of the December-January-February (DJF) mean ridged ice production rates from the CTRL run along with the differences with the three other model runs. Ridged ice production represents the volume of sea ice produced during ridging and rafting events. In addition, Fig. 13 shows the DJF mean thermodynamic ice growth rates from the CTRL run and the differences with the three other model runs. Thermodynamic ice growth in LIM3 consists of bottom ice growth and lateral ice formation. The ridged ice production and the thermody-

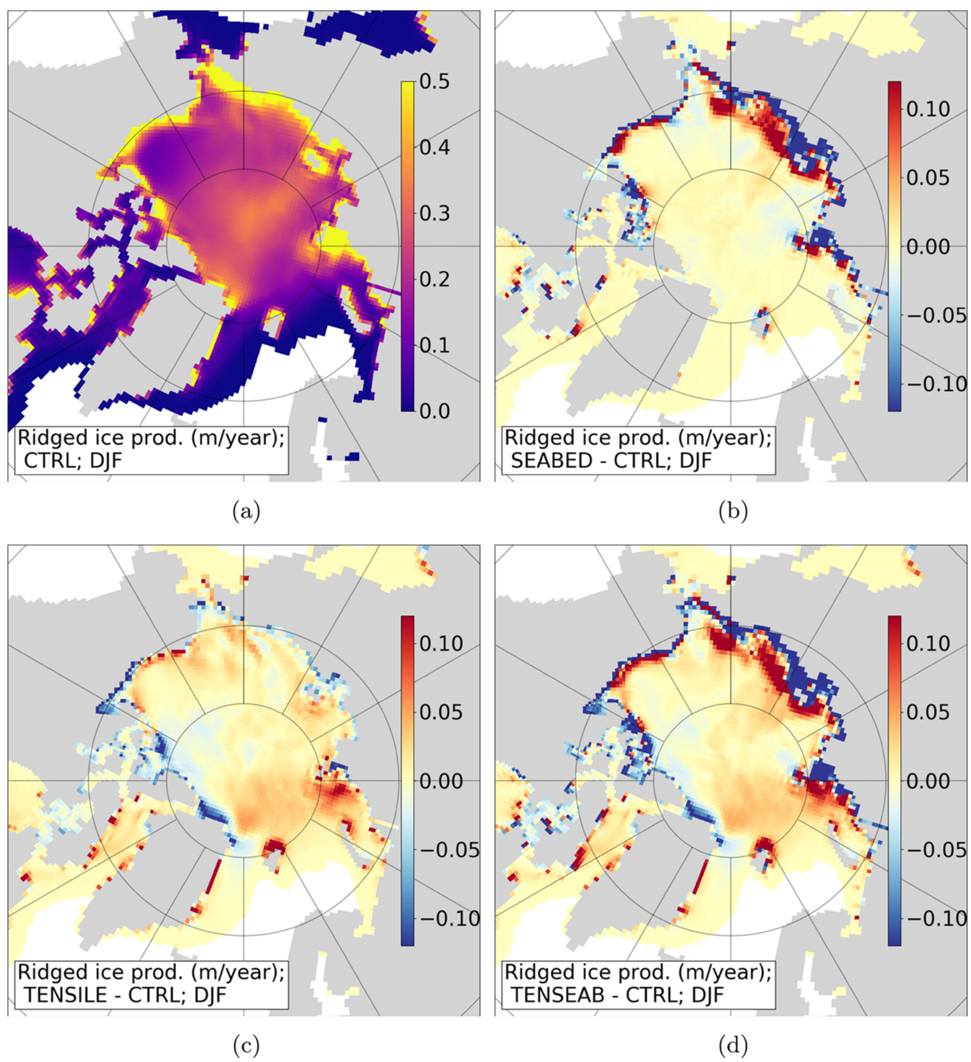

Fig. 12 Same as in Fig. 10, but for the mean December–January–Feburary (DJF) ridged ice production rates (m/year)

namic ice growth rates are particularly active in most coastal regions of the Arctic in DJF (Figs. 12a and 13a). Hence, these production rates are sensitive to the representation of landfast ice.

In the Laptev Sea, prevailing winds blowing offshore inhibit the piling of sea ice and the formation of pressure ridges in coastal areas, making the landfast ice surface smoother and less deformed in deep waters (Reimnitz et al. 1994). Landfast ice grows mainly thermodynamically in the coastal regions of Siberia, limiting its mean thickness to ∼1.6m in winter (Li et al. 2020). The SEABED run presents a lower ridged ice production than the CTRL run towards the coast of the LESS (Fig. 12b). In addition, the seabed stress scheme reduces the thermodynamic ice growth rates in these regions (Fig. 13b). Low deformation and thermodynamical ice growth rates are in agreement with the simulation of landfast ice along the coast of Siberia by the seabed stress scheme. The reduced thermodynamic ice growth and ridged ice production rates explain the thinner landfast ice cover simulated with this scheme.

In the flaw polynyas of the Laptev Sea, the continuous advection of cold Siberian air masses over the open water areas produces a high volume of sea ice in winter (Reimnitz et al. 1994; Morales Maqueda et al. 2004). Sea ice produced in the flaw polynyas (and parts of the landfast ice) is advected in the Transpolar Drift Stream across the Arctic Basin to Fram Strait. With the seabed stress scheme, the sites along Siberia with high thermodynamic ice growth rates move to offshore locations in winter (Fig. 13b). However, the sea ice volume produced in these offshore sites in the SEABED run is less important than the sea ice volume produced close to the Siberian coast in the CTRL run. As a result, the SEABED run presents a thinner sea ice cover than the CTRL run offshore of the Siberian coast (Fig. 11b). Eventually, sea ice velocity advects this thinner sea ice cover modelled with the seabed stress scheme in the Central Arctic (Fig. 14).

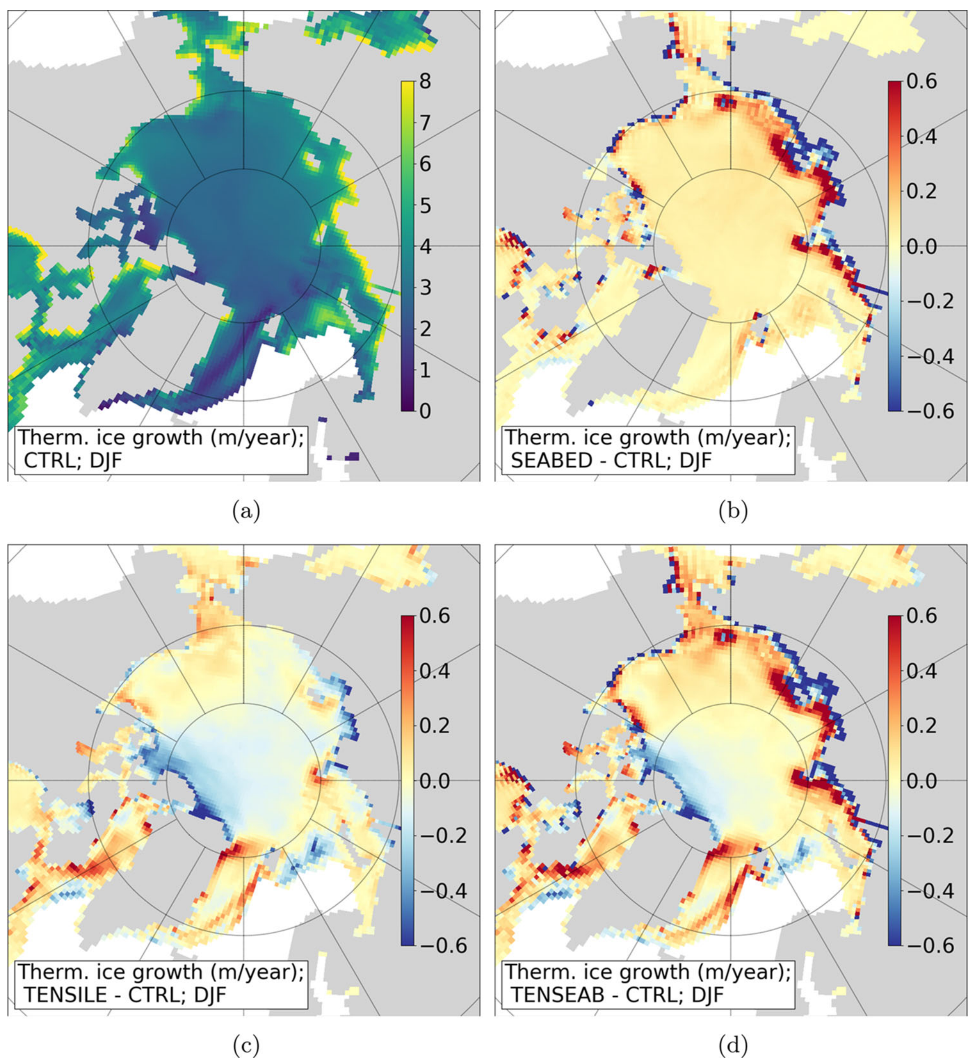

Fig. 13 Same as in Fig. 10, but for the mean December–January–Feburary (DJF) thermodynamic (bottom and lateral) ice growth rates (m/year)

The relocation of the high thermodynamic ice growth sites in the SEABED run impacts the simulated ice-ocean salt fluxes (not shown). In winter, the positions of the maxima in ice-ocean salt fluxes shift from the Siberian coast in the CTRL run to approximately above the continental shelf break in the SEABED run. These effects of the modelled landfast ice on sea ice production and salt fluxes agree with the results of Itkin et al. (2015).

3.2.2 Impact of the sea ice tensile strength scheme on sea ice conditions

The sea ice tensile strength scheme impacts the simulated Arctic sea ice thickness all year round (Fig. 11c). The modelled sea ice thickness is 10–30 cm larger in most of the Arctic with sea ice tensile strength. This effect is highest in the region north of Greenland and the CAA. Note that the simulated ice thickness is a little smaller in the Beaufort Sea with the sea ice tensile strength scheme.

The annual mean sea ice speed in the TENSILE run is ∼1cm/s smaller than in the CTRL run (Fig. 14c). The slowdown of the ice pack when including tensile strength is more pronounced in winter when sea ice is not in a free drift state (Fig. 6g). This slowdown reduces an existing overestimation in the mean Arctic sea ice speed during March compared to the NSIDC-drift observations from 2.7 cm/s for the CTRL run to 1.1 cm/s for the TENSILE simulation. The mean sea ice speed from the IABP buoys is ∼0.6cm/s higher than in the NSIDC-drift product during March (Docquier et al. 2017).

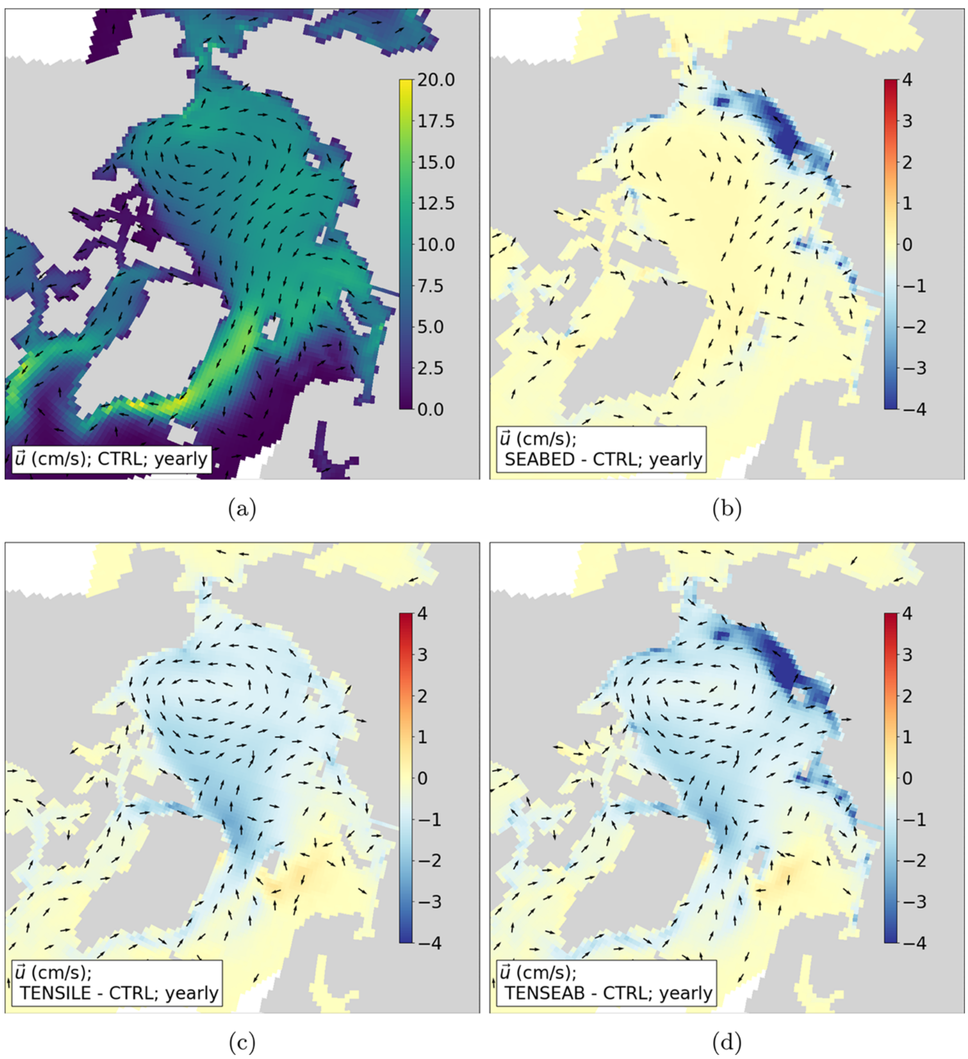

Fig. 14 Same as in Fig. 10, but for the annual mean sea ice drift. The arrows indicate the direction of the vectors. The colour map shows the magnitude of the vectors (cm/s). In the difference maps (b–d), the vectors whose magnitude is less than 0.05 cm/s are masked

Further analyses are required to confirm the reduced bias in the modelled winter mean sea ice speed when including tensile strength.

Zhang and Rothrock (2005) noted that prescribing fat yield curves (e.g., $e < 2$) and including isotropic tensile strength ($k_t > 0$) tend to decrease sea ice drift and increase sea ice thickness in most of the Arctic. The slowdown of the ice pack is expected from the increase in tensile strength properties. Indeed, decreasing e and increasing k_t result in higher shear strengths (Lemieux et al. 2016), meaning that sea ice can withstand more shear stress before plastic deformation. In turn, higher shear strengths are associated with lower sea ice speeds (Hibler 1979; Ip et al. 1991; Lemieux et al. 2016).

The less mobile ice pack modelled with the tensile strength scheme likely increases the lifespan of sea ice in the Arctic Basin. In addition, this scheme increases ridged ice production rates nearly everywhere in the Central Arctic, with the notable exception of the coastal regions of Greenland and the CAA (Fig. 12c). Zhang and Rothrock (2005) reported similar effects on their modelled ridged ice production rates when selecting fat yield curves with isotropic sea ice tensile strength. To some degree, the increased ridged ice production rates in the Central Arctic allow sea ice to grow thicker during an extended period while being advected in the Arctic Basin.

In our model runs, thick sea ice collects in the region north of the CAA and Greenland before exiting the Arctic Basin through the Fram Strait (Fig. 11) in relation to the large-scale sea ice motion in the Arctic (Fig.!14). The simulated sea ice velocity is small in the region north of the CAA and Greenland in the CTRL run (Fig. 14a). Including sea ice tensile strength further accentuates the loss of mobility of the sea ice cover in this region (Fig. 14c). As a result, the tensile strength scheme facilitates the accumulation of thick sea ice. Further, the TENSILE run displays reduced ridged ice production rates north of the CAA and Greenland compared to the CTRL run (Fig. 12c). This indicates the formation in the TENSILE run of a large static arch consisting of thick ridged ice in this region. Thick sea ice in this area may either flow westward towards Fram Strait or eastward along the northern coast of the CAA and enter the Beaufort Gyre, following the mean Arctic sea ice motion.

In the study of Zhang and Rothrock (2005), the ice volume export through the Fram Strait decreases when using fatter yield curves, including isotropic sea ice tensile strength, or both, because of the reduced sea ice velocity. In our model configuration, the average (1980–2015) annual sea ice volume export through the Fram Strait is -2.83e3km^3 in the CTRL run and -2.83e3km^3 in the TENSILE run. This little difference between the two model runs arises from the compensating effects of the increased sea ice thickness in the western Arctic and the reduced sea ice speeds through the Fram Strait when including the tensile strength scheme.

In the TENSILE run, the winter thermodynamic ice production is smaller than in the CTRL run in the Central Arctic and the region north of the CAA and Greenland (Fig. 13c). The thick ice cover simulated in the TENSILE run damps the growth and melt of sea ice and reduces the ice-ocean salt fluxes between the ice and ocean systems (not shown). This effect is greater north of Greenland and the CAA, where the salt fluxes reduce by 15 to 30 % in the simulations using the sea ice tensile strength scheme. In the Kara, Laptev, and East Siberian Seas, the relative differences in thermodynamic ice production between the CTRL and TENSILE runs are less than 5 % in winter. Consequently, the impact of the tensile strength scheme on the ocean–ice salt fluxes is less significant during winter in these regions.

3.2.3 Effect of the two landfast schemes on sea ice conditions

The impact of the seabed stress scheme in the TENSEAB run on the simulated sea ice state is evident in the Siberian shelf regions. In these regions, the TENSEAB run presents thinner sea ice than the CTRL run, with local exceptions in the proximity of the coast (Fig. 11d). These differences are consistent with the reduced thermodynamic ice growth and ridged ice production caused by the simulation of landfast ice, as described for the SEABED run (Section 3.2.1). Moreover, the June-July-August mean sea ice concentration difference between the TENSEAB and CTRL runs (Fig. 10d) is close to the difference between the SEABED and CTRL in the LESS (Fig. 10b). As for the SEABED run, the simulation of landfast ice in the TENSEAB run enhances (delays) the melting of sea ice offshore (onshore) in the LESS. Lastly, the annual mean sea ice drift from the TENSEAB run significantly reduces in the LESS (Fig. 14d), where the frequency of occurrence of landfast ice is high (Fig. 4d).

The signature of the sea ice tensile strength on the simulated sea ice cover is visible in most of the Central Arctic. Indeed, the TENSEAB run presents, compared to the CTRL run, a thicker (Fig. 11d), slower (Fig. 14d) and more consolidated (Fig. 10d) Arctic sea ice cover. These differences in the simulated sea ice conditions increase towards the American Continent as what we described for the TENSILE run (Section 3.2.2). The thicker sea ice cover simulated in the TENSEAB runs is linked to lower thermodynamic ice growth rates compared to the CTRL run (Fig. 13d). Additionally, the ridged ice production increases in most of the Arctic when including the sea ice tensile strength scheme (Fig. 12d).

The simulation in the TENSEAB run of the signatures from the sea ice tensile strength and seabed stress schemes is possible for the reason that these two schemes target specific sea ice processes, namely, seabed–ice keel interactions and sea ice tensile strength properties. These processes can interact, enabling the simulated landfast ice cover to expand further. For instance, the grounding of ice ridges may act as anchoring platforms from which sea ice arches may attach, thanks to the non-zero sea ice tensile strength properties. As a result, we anticipate a non-linear effect of these two schemes on the simulated landfast ice cover and hence on sea ice conditions. To investigate these effects, we compare the sum of differences or anomalies from the TENSILE and SEABED runs with respect to the CTRL run with the equivalent from the TENSEAB run compared to the CTRL run. This comparison is a preliminary assessment of the additive property of the effects of the landfast ice process schemes. A comprehensive analysis of the non-linearities would require examining both the additivity and homogeneity (scaling) properties of the impact of these two schemes. We consider such an analysis beyond the scope of the present study. Lastly, we limit ourselves to the modelled sea ice thickness and velocity. The impact of the non-additivity on the simulated sea ice concentration is relatively small (less than 10 %) and limited to summer months.

Combining the sea ice tensile strength and seabed stress schemes further slows the sea ice motion in the LESS compared to the sum of the individual actions of these schemes on sea ice drift (Fig. 15a). These non-additive differences amount to ∼0.7cm/s against ∼5cm/s for the difference in sea ice drift between the TENSEAB and CTRL runs (Fig. 11d). They are associated with more frequent occurrences of landfast ice in winter (Fig. 4d) and a positive difference in sea ice concentration during JJA (Fig. 10d). Note the simulated sea ice drift in the CAA is low and nearly equal in our four model runs. Consequently, the non-additivity effect of the landfast ice process schemes on the sea ice drift is weak in this region. Otherwise, the ice velocities from the TENSEAB run are close to those from the TENSILE simulation in the Central Arctic.

The non-additive effects of the two landfast ice process schemes on the modelled sea ice thickness principally confine to the LESS and CAA and some of their neighbouring regions (Fig. 15b). In the LESS, the sum of the ice thickness anomalies from the SEABED and TENSILE runs exceeds the equivalent anomalies from the TENSEAB run, with the CTRL run as a reference. Indeed, activating both landfast ice process schemes damps sea ice motion and thus enhances the sea ice thinning effect of the modelled landfast ice cover along Siberia. These non-additive ice thickness differences in the LESS (∼15cm) are within the order of magnitude of the ice thickness differences between the SEABED (TENSILE) and CTRL runs.

In the CAA, the association of the two landfast ice process schemes leads to spatially heterogeneous non-additive effects on the sea ice thickness. We note that the thinning effects of the two landfast ice process schemes in the interior of the CAA are enhanced when these schemes are combined. However, the simulated landfast ice extent in the CAA in the TENSEAB run overestimates the NIC observations and all our other model runs all year round (Fig. 5d). Based on the results of Lemieux et al. (2018), we recommend investigating the sensitivity of sea ice to landfast ice process parameterizations in the CAA conjointly with the effect of tides. The ice thickness anomalies shown in Fig. 15b suggest that the non-linear effects are significant in the CAA in regard to the mean sea ice thickness simulated in the CTRL run. It shows the importance of landfast ice processes for modelling sea ice in the CAA.

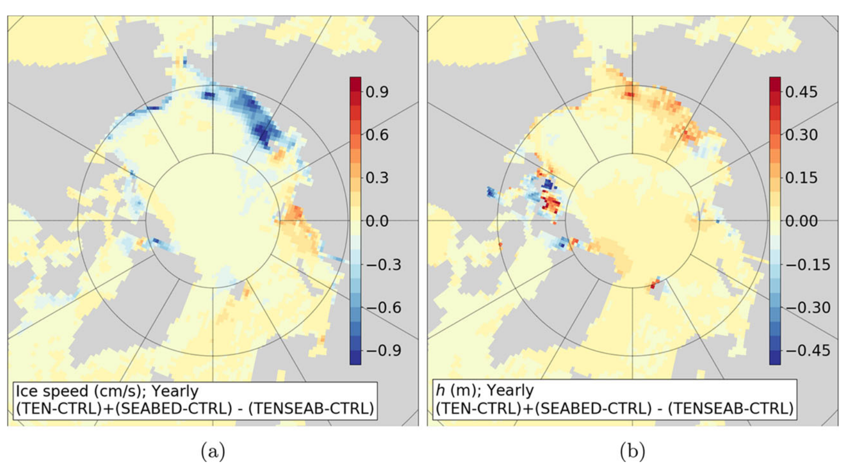

Fig. 15 Differences between the sum of the anomalies from the TENSILE and SEABED runs and the equivalent anomaly from the TENSEAB run with the CTRL run as a reference for the annual mean sea ice speed (a) and thickness (b) over 1980–2015

3.3 Arctic halocline sensitivity to the landfast ice process schemes

3.3.1 Effect of the seabed stress scheme on the Arctic Ocean

The simulation of landfast ice and the new location of flaw polynyas in the SEABED run strongly impacts the properties of shelf waters along the coast of Siberia. This impact is clear in the transects showing the differences in ocean potential temperature and salinity between the SEABED and CTRL runs (Fig. 16). Landfast ice shields seawater from the atmosphere in winter. This shielding effect allows freshwater released by river runoff to accumulate on the shelves in winter (Itkin et al. 2015). Moreover, ice-ocean salt fluxes decrease in landfast ice-covered regions owing to lower thermodynamic ice growth rates (Fig. 13b). This further reduces the ocean salinity in the coastal shelf regions of Siberia (Fig. 16a and b). Landfast ice enables relatively cold waters to remain on the continental shelves in spring. Later, these cold waters delay the melting of the landfast ice cover during the melt season in the simulations using the seabed stress scheme (Fig. 16c and d). Hence, the simulated Siberian shelf waters in the SEABED run are fresher and thus less dense (although colder) than the ones in the CTRL run.

The low sea ice concentration in flaw polynyas promotes ocean heat gain from solar radiation in spring and summer and brine rejection from sea ice growth in fall and winter. As a result, the water column at the shelf break along Siberia tends

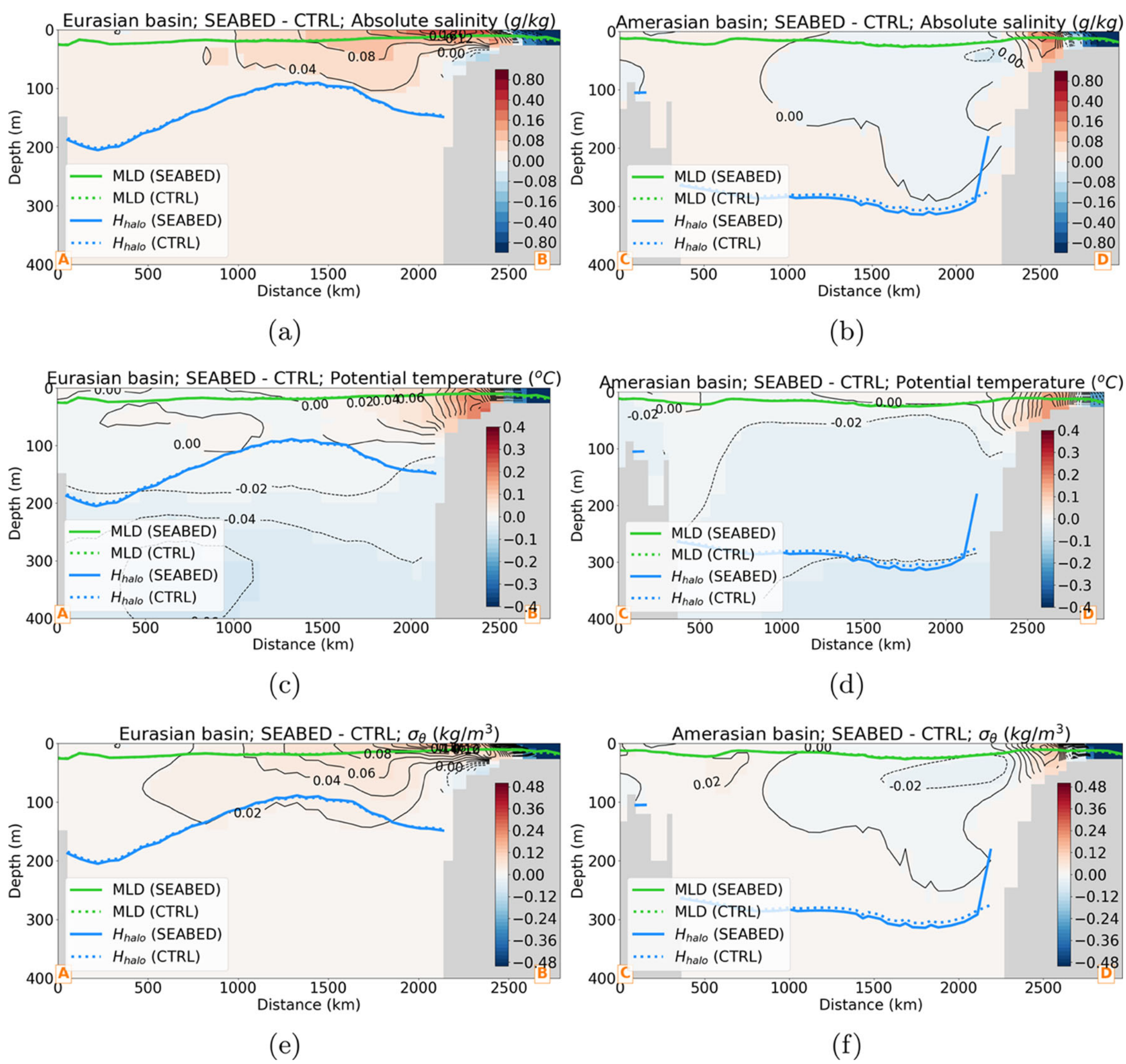

Fig. 16 Differences in the annual mean (1980–2015) ocean salinity (a, b), potential temperature (c, d) and σ_θ (e, f) between the SEABED and CTRL model simulations along the transects AB across the Eurasian Basin (a, c, e) and CD across the Amerasian Basin (b, d, f). The blue and green lines indicate the depth of the mixed layer and the lower boundary of the halocline layer, respectively. Continuous (dotted) lines correspond to the SEABED (CTRL) run. Figure 1 shows the position of the oceanic transects

to be warmer and more saline when the seabed stress scheme is activated. These changes in water properties weaken the vertical stratification in the Siberian shelf break regions.

The Transpolar Drift Stream follows a route roughly parallel to line AB displayed in Fig. 1. This oceanic stream transports the water mass properties from the Laptev Sea to the interior of the Eurasian Basin. Thus, with the seabed stress scheme, the warmer and more saline water mass originating from flaw polynyas tends to propagate into the interior of the Eurasian Basin. This moderately increases the density in the Eurasian Basin and results in a weaker stratification in this basin.

In the Amerasian Basin, the water masses created by the flaw polynyas along the coast of Siberia are advected anticyclonically in the Beaufort Gyre or carried in the Transpolar Drift Stream towards Fram Strait. In the SEABED run, this water mass is warmer and more saline than the one from the CTRL run. These modelled temperature and salinity differences reduce while being advected along the margins of the Amerasian Basin. The signature of these differences can be seen on the salinity transect across the Amerasian Basin CD (Fig. 16b), in the East Siberian Sea where they originate, and near the CAA after the reduction of these differences. The upper layer of the halocline in the center of the Beaufort Gyre is fresher when using the seabed stress scheme. This difference leads to a moderately strengthened halocline stratification in the Beaufort Gyre.

Itkin et al. (2015) examined the stability of the Arctic water column from the sea surface down to the upper surface of the halocline layer (down to 50 m). These authors found a significant sensitivity of the halocline stability at its upper boundary to the simulated landfast ice cover. Namely, they reported that improving the representation of landfast ice enhances the halocline stability in the Canada Basin. This strengthening is a consequence of the freshening of the surface mixed layer and salinification of the halocline layer. The former relates to changes in river runoff, whereas the latter is due to differences in the dense water production of flaw polynyas. On the other hand, they reported for the Makarov and Eurasian Basins a weakening effect of landfast ice for the halocline stability due to increased ocean salinities. Our results agree to some degree with the conclusions of Itkin et al. (2015). Overall, the impact of the seabed stress scheme on the stability of the Arctic halocline is weak in our model setup. Although the salinity along the transects across the Eurasian and Amerasian Basins are slightly different between the SEABED and CTRL runs (Fig. 16a and 16b), the resulting density differences between these two runs are minor (Fig. 16e and 16f). The little density differences between the SEABED and CTRL runs in the upper part of the halocline layer are related to the weak increase of $27 \mathrm{kJ/m^2}$ or 3 % in APE in the Amerasian Basin (Fig. 17b). An increase in the APE corresponds to a stronger ocean stratification. Otherwise, the differences in APE between the SEABED and CTRL runs are close to zero in the Eurasian Basin.

Itkin et al. (2015) redistributed the 36 vertical levels of their model grid to increase the resolution towards the surface. This approach allowed for a better representation of surface processes but at the price of deep ocean physics. In addition, these authors reduced the vertical background diffusivity of the k-profile vertical mixing scheme in their model setup. In doing so, they aimed to improve the simulation of the upper halocline layer (Nguyen et al. 2009). These two adjustments have not been considered in our model study. The double hyperbolic tangent function defining the 75 vertical levels of NEMO-LIM3 is kept unchanged in our setup as a trade-off for the resolution of surface and deep ocean processes. We left the tuning of the turbulent kinetic energy (TKE) vertical mixing scheme for the Arctic and sub-Arctic regions open for future model studies. These choices allow us to examine the impact of the seabed stress scheme on the stability of the Arctic halocline layer over its entire thickness without interfering with the current model tuning of the World Ocean. Realistic brine rejection parameterizations may also help improve the representation of the Arctic halocline layer (Nguyen et al. 2009; Barthélemy 2016).

The influence of the modelled landfast ice on the APE of the Arctic halocline depends on the choice of the landfast ice process scheme (Fig. 17). As described in Section 3.1.1, TENSEAB and SEABED exhibit occurrences of landfast ice close to the NIC observations (Figs. 4 and 3). Despite the improved representation of landfast ice in these two model runs, the differences in the simulated APE between the TENSEAB and CTRL runs (Fig. 17d) do not correspond to the equivalent differences between the SEABED and CTRL runs (Fig. 17b). This suggests that the landfast ice modelled with the seabed stress scheme plays a lesser role in the stability of the Arctic halocline layer than the one played by the sea ice tensile strength scheme in our model setup.

3.3.2 Effect of the sea ice tensile strength scheme on the Arctic Ocean

The large-scale atmospheric circulation in the Arctic impacts the freshwater distribution in the upper ocean on time scales of several years to decades (Timmermans and Marshall 2020). In particular, a weak Arctic high-pressure system is associated with a low freshwater content in the Beaufort Gyre and a freshwater transfer from the Beaufort Gyre to the Eurasian basin and vice versa (Timmermans et al. 2011). Although our model runs share the same atmospheric forcing, the differences in sea ice properties between the simulations can alter the freshwater content in the upper ocean. The sea ice tensile strength scheme leads to an increased (decreased) salinity in the halocline layer of the Amerasian (Eurasian) Basin (Fig. 18). These distinct regional effects on the halo-

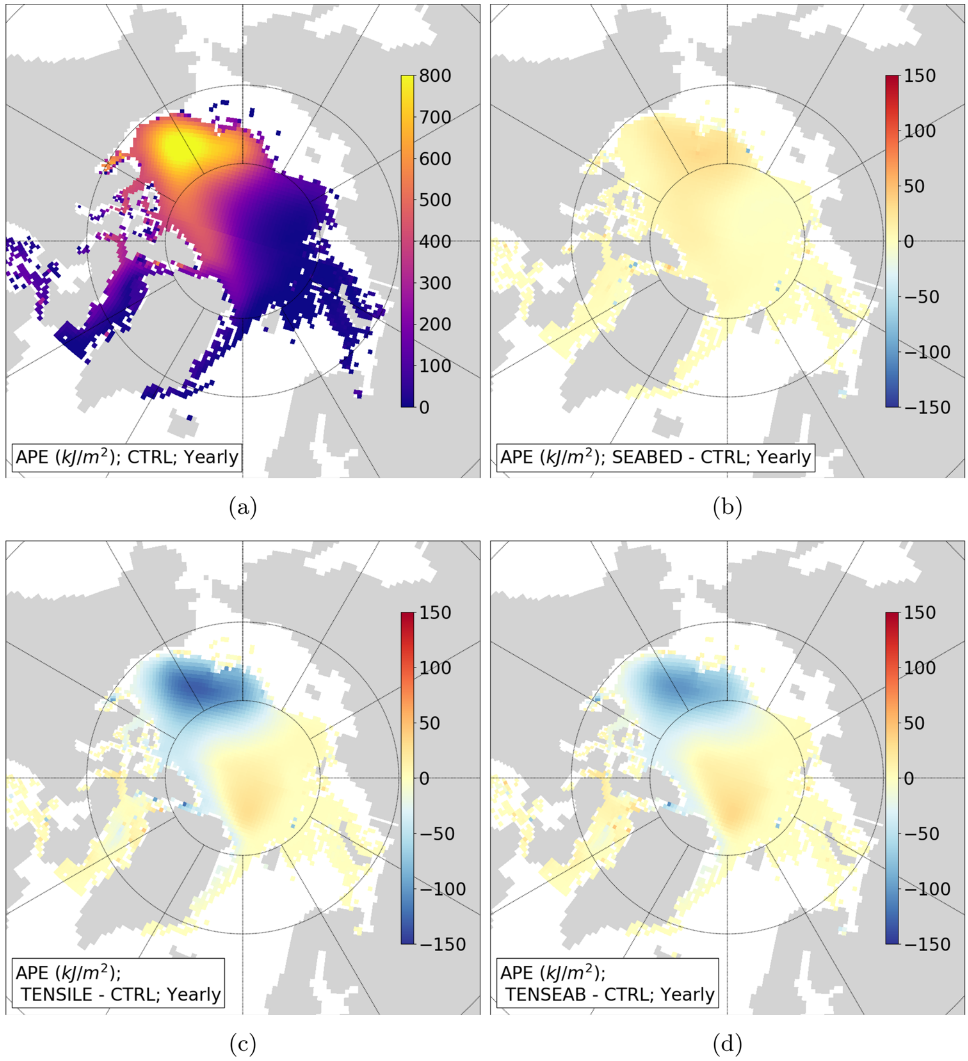

Fig. 17 Annual mean (1980–2015) available potential energy (APE) (kJ/m^2) integrated from the surface down to H_{halo} from the CTRL run (a), and APE differences between the SEABED (b), TENSILE (c), TENSEAB (d) runs with the CTRL run as a reference. The APE is calculated for latitudes greater than 60 °N where sea ice concentration is at least 15 %. Note that (a) is identical to Fig. 9

cline salinity originate from the impact of the scheme on the Arctic sea ice state. In the TENSILE run, the modelled sea ice is less mobile, thicker, and more consolidated than in the CTRL run. These changes generate a more efficient decoupling between the atmosphere and ocean, limiting the direct action of wind stress on the sea surface.

The less mobile ice pack enhances the importance of ocean surface currents for ocean surface stress. In the Beaufort Gyre, these changes reinforce the role of the ice–ocean stress governor mechanism in turning off the Ekman pumping (Meneghello et al. 2018a). This mechanism describes the self-regulation of the Beaufort Gyre spin-up. When the Beaufort Gyre tends to equilibrium, the relative velocities between sea ice and ocean surface reduce, leading to lower ocean surface stress and lower Ekman pumping rates. As a result, the annual mean Ekman downwelling rate simulated in the center of the Beaufort Gyre is lowered from 17 m per year in the CTRL run to 13 m per year in the TENSILE run. The less efficient Ekman downwelling caused by the sea ice tensile strength scheme reduces the freshwater content of the Beaufort Gyre. Observations in the Beaufort Sea give 25 m per year for the spatial maximum in the annual mean (1979–2014) Ekman downwelling rate (Ma et al. 2017). For reference, Meneghello et al. (2018b) estimated the average Ekman downwelling rate in the Beaufort Gyre region as 2.3 m per year over 2003–2014.

The weaker Beaufort Gyre allows for the release of freshwater into the Eurasian Basin, leading to the freshening of the halocline layer in this basin (Timmermans et al. 2011). Thus, the less efficient Ekman downwelling simulated in the TENSILE run likely explains the freshening of the halocline in the Eurasian Basin. In addition to this mechanism, the thicker ice cover modelled using the sea ice tensile strength scheme is associated with decreased thermodynamic ice growth rates in winter (Fig. 13c). The negative difference in the DJF thermodynamic ice growth rates between the TENSILE and CTRL runs accentuates in the Eurasian Basin towards Greenland. This causes a reduction in the brine rejection rates (not

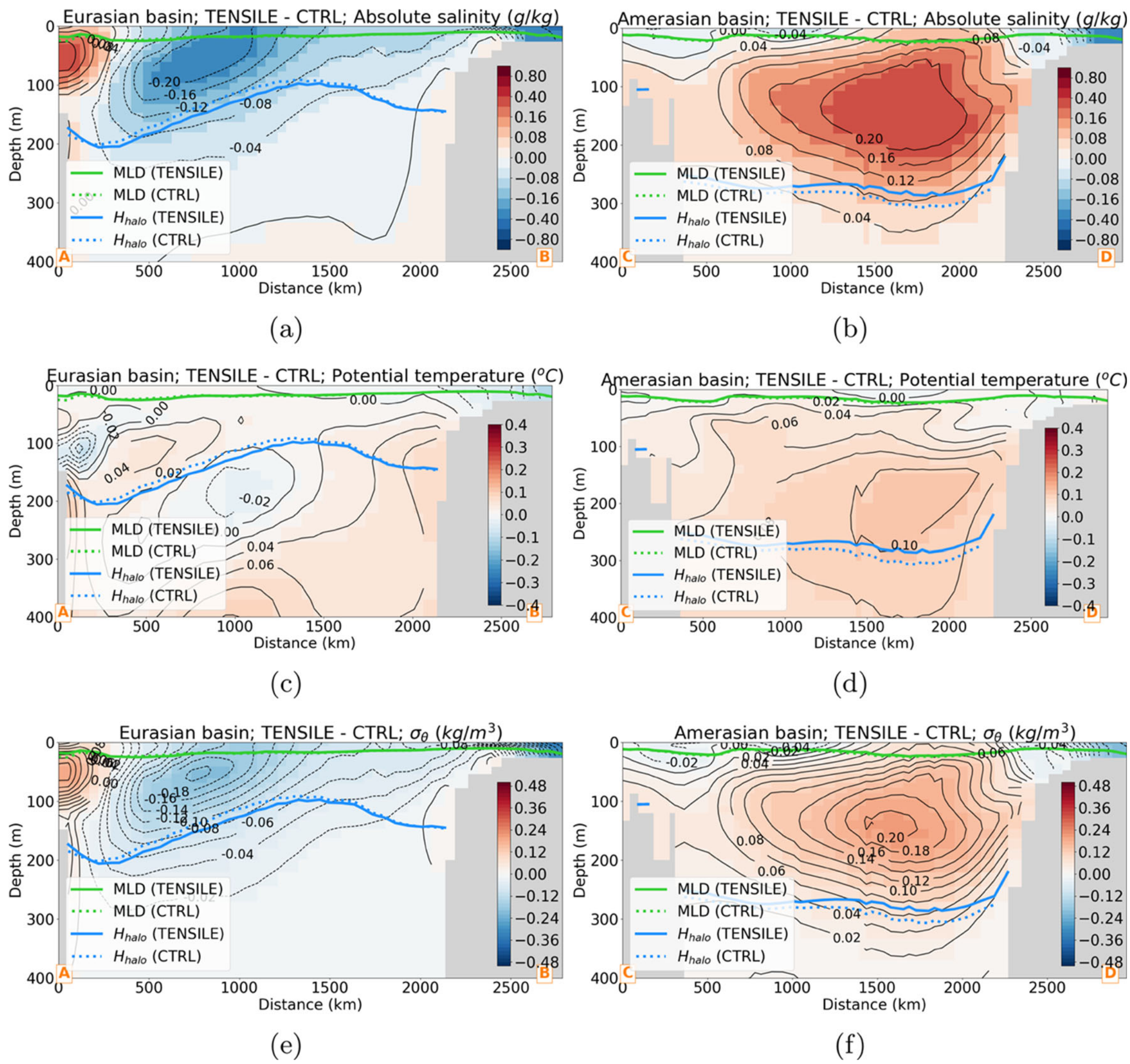

Fig. 18 Same as Fig. 16, but for the differences between the TENSILE and CTRL runs

shown) and a less efficient salinification of the ocean surface in winter. The Transpolar Drift Stream accentuates the negative salinity differences between the TENSILE and CTRL runs by advecting water mass property anomalies towards Fram Strait.

The re-stratification of the halocline layer in the Eurasian Basin when activating the sea ice tensile strength scheme is opposed to the "Atlantification" of the Arctic Ocean (e.g., Polyakov et al. 2017). The latter is a process whereby a weakened stratification of the Arctic Ocean enables the intrusion of Atlantic water into the polar surface mixed layer. The associated ocean heat fluxes promote sea ice loss, higher exchanges between the upper ocean and the atmosphere, and deeper winter ventilation. In the TENSILE run, the modified sea ice state is responsible for the enhanced stability of the halocline layer in the Eurasian Basin. The strengthened stratification of the halocline layer prevents the intrusions of Atlantic water into the surface mixed layer. These changes limit deep winter convection in the TENSILE run.

The shielding effect of shelf waters by landfast ice in the coastal regions of Siberia is less efficient in the TENSILE run than in the SEABED run. Contrary to the SEABED run, the TENSILE simulation does not feature increased ocean potential temperature and salinity in the water column above the Siberian shelf break (Fig. 18). The little impact of the sea ice tensile strength scheme on the Siberian shelf water properties relates to the simulation of landfast ice with this scheme. In the TENSILE run, the occurrences of landfast ice are less frequent along the Siberian coast than in the NIC observations or the SEABED run. This underestimation prevents shifting the boundary between landfast ice and drift ice to an offshore position. Thus, the locations of the winter sea ice production, brine rejection, and summer ocean heat absorption in the TENSILE run are closer to the CTRL run than those of the SEABED run.

The sea ice tensile strength scheme influences the depth H_{halo} of the base of the Arctic halocline layer. In the TENSILE run, this depth is 20 m greater in the western Eurasian Basin but 30 m smaller in the Amerasian Basin compared to the CTRL run. These changes in H_{halo} between the two model runs essentially arise from the differences in the simulated Arctic halocline salinity. The fresher (more saline) halocline layer simulated in the Eurasian (Amerasian) Basin with sea ice tensile strength leads to a deeper (shallower) transition between the stratification regimes ($R_\rho = 0.05$). These differences in halocline salinity influence the simulated density anomalies used for calculating the APE. In the Eurasian (Amerasian) Basin, these density anomalies are lower (higher) in the TENSILE run than in the CTRL run, owing to the fresher (more saline) halocline layer. Consequently, the APE simulated with the sea ice tensile strength scheme is $\sim$130kJ/m^2 lower in the Amerasian Basin but $\sim$30kJ/m^2 higher in the Eurasian Basin (Fig. 17). The sea ice tensile strength scheme moderately reduces the gap in the APE simulated with our model configuration and observations from the PHC climatology in the Beaufort Sea.

The association of the seabed stress scheme to the tensile strength scheme in the TENSEAB run does not yield significant additional differences in APE compared to the TENSILE run (Fig. 17). Indeed, the spatial distribution of the differences in the modelled APE between the TENSEAB and CTRL runs (Fig. 17c) is similar to the equivalent differences between the TENSILE and CTRL runs (Fig. 17d). This demonstrates that the tensile strength scheme has more influence on the Arctic halocline stability than the seabed stress scheme. In our simulations, the indirect impact of sea ice tensile strength on the Arctic halocline stability via the modelled sea ice state exceeds the direct effect of landfast ice on this ocean layer.

4 Conclusion

In this paper, we investigated with the global, coupled ocean–sea ice model NEMO-LIM3 the importance of the landfast ice representation for the simulation of the Arctic sea ice cover and its influence on the stability of the Arctic halocline. We implemented two conceptually different landfast ice process schemes to refine the representation of Arctic landfast ice in this model. The first scheme prescribes a seabed stress term in the ice momentum equation to simulate the effect of grounded ice ridges on the seafloor (Lemieux et al. 2015). The second scheme modifies the ice rheology to include isotropic tensile strength and increases uniaxial tensile strength (König Beatty and Holland 2010). We assessed the ability of the model to simulate the Arctic landfast ice cover using landfast ice observations (1980–2015) derived from the NIC sea ice charts (Fetterer and Fowler 2006; Dupont et al. 2022). The novelty of this research is that, in addition to the landfast ice assessment, we examined the effects of this type of ice on the whole sea ice pack and the stability of the Arctic halocline layer over its entire thickness.

As a reference to the scientific community, the following enumerated paragraphs present the outcomes of this study. In addition, Fig. 19 summarises these findings graphically as an organizational chart.

1. NEMO-LIM3 simulates relatively well the landfast ice extent in the CAA by default, albeit this requires a sufficiently high number of EVP sub-iterations (equal to 920 in this study). The simulated landfast ice state improves when combining the tensile strength scheme with the seabed stress scheme. However, this combination still underestimates the observed occurrence frequencies of landfast ice in deep water regions, such as in the Kara Sea. These findings confirm the suitability of the EVP algorithm for simulating ice arches in the CAA, the role of grounded ice ridges in the development of landfast ice in the shallow Siberian shelf waters (Lemieux et al. 2015), and the importance of sea ice tensile strength for Arctic landfast ice (Lemieux et al. 2016).
2. Improving the simulation of landfast ice leads to a shift in the position of low sea ice concentration areas. With the seabed stress scheme, the boundary between drift ice and landfast ice moves offshore to a new location situated approximately above the Siberian shelf break. These regions with low sea ice concentrations are hotspots for oceanic heat gain in summer and ice growth in winter (Morales Maqueda et al. 2004). On the other hand, landfast ice shields seawater from interactions with the atmosphere (Itkin et al. 2015). Furthermore, landfast ice limits the production of sea ice volume by inhibiting sea ice deformation (Fig. 12b) and damping thermodynamic sea ice growth (Fig. 13b). Therefore, our model runs using the seabed stress scheme tend to simulate 1) warmer and more saline water masses near the Siberian shelf break and 2) colder and fresher water masses in the Siberian shelf regions. These changes in ocean and sea ice properties promote summer sea ice melt at the Siberian shelf break and delay landfast ice melt above the Siberian shelves.
3. Modifying the sea ice rheology formulation to increase the tensile strength significantly impacts the modelled Arctic sea ice state. The Arctic sea ice cover is thicker, more consolidated, and less mobile with sea ice tensile strength. These changes are expected due to the higher resistance to shear forces when lowering the eccentricity of the elliptical yield curve ($e < 2$) and including

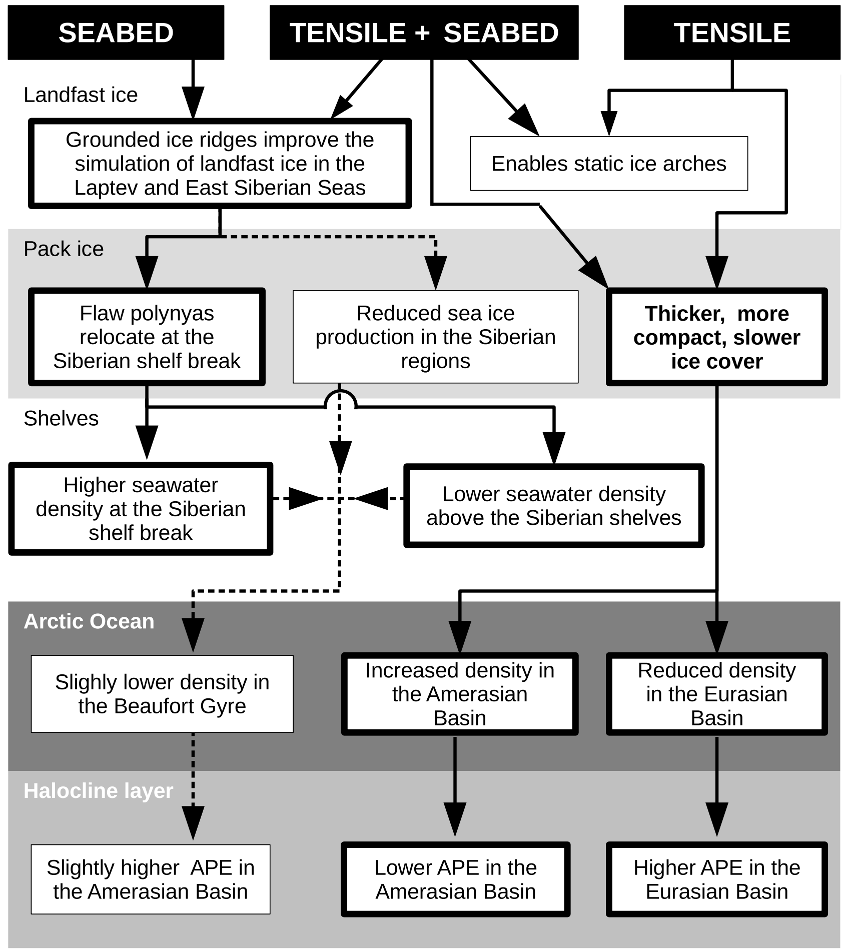

Fig. 19 Organization chart presenting the principal effects of the seabed stress scheme (SEABED), the sea ice tensile strength scheme (TENSILE), and their association (TENSILE + SEABED) on the Arctic landfast ice and sea ice cover, the Siberian shelve waters, the Arctic Ocean and the Arctic halocline layer properties. Text in bold, thick arrows, and thick lines (regular text, dashed arrows, and thin lines) indicate strong (weak) relationships

isotropic tensile strength ($k_t > 0$). The thicker ice pack modelled with the tensile strength scheme reduces basal ice growth and brine rejection rates in winter. The sea ice tensile strength scheme reduces an existing bias in the simulated winter sea ice speed by 1.7 cm/s compared to the NSIDC-drift product (Tschudi et al. 2019) (Fig. 6g, h). On the other hand, this scheme increases the positive difference in total sea ice volume between the CTRL run and the PIOMAS dataset (Zhang and Rothrock 2003; Schweiger et al. 2011). Generally, we may not conclude whether the implemented landfast ice process schemes improve or degrade sea ice drift or the total Arctic sea ice volume because of uncertainties in the NSIDC-drift dataset (Sumata et al. 2015; Szanyi et al. 2016) and the PIOMAS product (Schweiger et al. 2011).

4. The influences of the seabed stress and tensile strength schemes on the stability of the Arctic halocline are distinct. The seabed stress scheme slightly strengthens the ocean stratification in the Amerasian Basin (APE is ~27kJ/m^2 higher) because of a fresher Beaufort Gyre and more saline water masses circulating anti-cyclonically in the Amerasian Basin. These changes in hydrography likely originate from the improved simulation of the landfast ice state and the boundary between drift ice and landfast ice in the Siberian regions. The sea ice tensile strength scheme weakens the stratification (APE is ~130kJ/m^2 lower) in the Amerasian Basin and strengthens it (APE is ~30kJ/m^2 higher) in the Eurasian Basin. These changes in the halocline stratification are a consequence of the effects of the tensile strength scheme on the Arctic sea ice conditions. The thicker and more consolidated ice pack modelled with this scheme gives more importance to the ice–ocean stress governor mechanism for turning off the atmospheric forcing of the Beaufort Gyre. The ice–ocean stress governor is a mechanism describing the negative feedback between the Ekman pumping and the relative ocean surface velocities in polar ocean gyres (Meneghello et al. 2018a). As sea ice drift and ocean surface velocities equalise, the ocean surface stress driving the Beaufort Gyre decreases, and the Ekman pumping tends towards zero. In the simulations using the sea ice tensile strength scheme, the less mobile ice pack attenuates the atmospheric forcing. This leads to a less effective freshwater accumulation in the Beaufort

Gyre and the likely freshwater transfer to the Eurasian Basin. Additionally, thick sea ice and reduced brine rejection rates reinforce the stability of the halocline layer in the Eurasian Basin. This effect of the sea ice tensile strength scheme is the opposite of the “Atlantification” of the Arctic Ocean (e.g., Polyakov et al. 2017).

Our simulations using the sea ice tensile strength scheme underestimate the landfast ice extent and frequency of occurrence in deep water regions. We may not exclude issues related to the difference in landfast ice definitions used for the model and the NIC observations. However, the underestimation of the modelled landfast ice extent contrasts with the past model studies of Olason (2016) and Lemieux et al. (2016). These authors successfully modelled landfast ice over deep water by increasing the maximum viscosity for the EVP algorithm (Olason 2016) or increasing the isotropic tensile strength (Lemieux et al. 2016). Our 1° horizontal model grid is likely missing key coastal features that could enable static ice arches and offshore extensions of landfast ice over deep water. Parameterizing subgrid-scale coastal information or resolving them using high-resolution models would likely help to simulate a more realistic landfast ice cover in our model setup. We could further improve the simulation of Arctic landfast ice by using a probabilistic method for the seabed stress scheme (Dupont et al. 2022). Lastly, we neglected the impact of tides on landfast ice in this study. Including this effect limits the overestimation of the landfast ice extent in tidal-active regions, such as the CAA (Lemieux et al. 2018).

We extended the study of Itkin et al. (2015) by examining quantitatively the effect of Arctic landfast ice on the stability of the halocline layer over its entire thickness. We used the APE as a bulk measure of this stability (Polyakov et al. 2018). In our simulations, the stability of the Arctic halocline layer is sensitive to the Siberian landfast ice cover but only to a small degree. The impact of the sea ice tensile strength scheme on the APE outpaces the corresponding effect of the seabed stress scheme on this quantity in either the Eurasian or Amerasian Basins (Fig. 17). The sea ice tensile strength scheme influences the Arctic sea ice velocity and thickness and, subsequently, the stratification of the Arctic halocline. The seabed stress scheme acts on the stability of this ocean layer via the representation of the landfast ice state.

The representation of the Arctic halocline layer would benefit from realistic brine rejection and vertical mixing schemes in our model setup (Nguyen et al. 2009; Barthélemy et al. 2015; Ilıcak et al. 2016). Furthermore, our simulation of the Arctic hydrography likely suffers from biases associated with the inflow of Atlantic water in the Arctic Basin and ocean shelf processes in the Siberian regions (Heuzé et al. 2023). Lastly, we may need to revisit our results with a fully coupled ocean–sea ice–atmosphere model setup. The coupling with the atmosphere is relevant in regard to the effects of landfast ice on the position of flaw polynyas (Morales Maqueda et al. 2004).

Acknowledgements The authors would like to thank Alain Caya from Environment and Climate Change Canada (ECCC) for providing the extended landfast ice observations (2008–2015) derived from the National Ice Center (NIC) sea ice charts. In addition, the research leading to these results has received funding from the European Commission’s Horizon 2020 APPLICATE (GA 727862) and PRIMAVERA (GA 641727) projects. Computational resources have been provided by the supercomputing facilities of the Université catholique de Louvain (CISM/UCLouvain) and the Consortium des équipements de Calcul Intensif en Fédération Wallonie Bruxelles (CÉCI) funded by the F.R.S.-FNRS under convention 2.5020.11.

Author Contributions Conceptualization: Jean Sterlin, Tim Orval, Thierry Fichefet; Methodology: Jean Sterlin, Jean-François Lemieux, Clément Rousset, Jonathan Raulier; Formal analysis and investigation: Jean Sterlin, Tim Orval, Thierry Fichefet, François Massonnet; Writing - original draft preparation: Jean Sterlin, Tim Orval, Thierry Fichefet, François Massonnet, Jean-François Lemieux, Clement Rousset, Jonathan Raulier; Writing - review and editing: To be determined; Funding acquisition: Thierry Fichefet, Francois Massonnet; Supervision: Thierry Fichefet, Francois Massonnet;

Data and code availability The sea ice velocity and concentration observations are distributed by the National Snow and Ice Data Center (NSIDC) (https://nsidc.org/data/nsidc-0116 and http://nsidc.org/data/nsidc-0051, respectively). In addition, the NSIDC distributes the National Ice Center (NIC) sea ice charts for the period 1980–2007 in gridded format (https://nsidc.org/data/G02172/versions/1). The extension of this product from 2008 to 2015 by Environment and Climate Change Canada (ECCC) is available upon request. The sea ice thickness from the Pan-Arctic Ice Ocean Modeling and Assimilation System (PIOMAS) can be accessed at http://psc.apl.washington.edu/zhang/IDAO/data_piomas.html. The Polar science center Hydrographic Climatology (PHC) in version 3.0 can be retrieved at http://psc.apl.washington.edu/nonwp_projects/PHC/Climatology.html. The four model runs examined in this study and the NEMO-LIM3 code used to generate them are available upon request.

References

Aagaard K, Coachman LK, Carmack E (1981) On the halocline of the Arctic Ocean. Deep-Sea Res I: Oceanogr Res Pap 28(6):529–545. https://doi.org/10.1016/0198-0149(81)90115-1 https://www.sciencedirect.com/science/article/pii/0198014981901151

Amante C (2009) ETOPO1 1 Arc-Minute Global Relief Model: Procedures. National Geophysical Data Center, NOAA, Data Sources and Analysis

Årthun M, Eldevik T, Smedsrud LH et al. (2012) Quantifying the influence of atlantic heat on Barents sea ice variability and retreat. J Clim 25(13), 4736–4743. https://doi.org/10/f34n39

Årthun M, Eldevik T, Smedsrud LH (2019) The role of atlantic heat transport in future Arctic winter sea ice loss. J Clim 32(11):3327–3341. https://doi.org/10.1175/JCLI-D-18-0750.1, https://journals.ametsoc.org/view/journals/clim/32/11/jcli-d-18-0750.1.xml

Barry RG, Moritz RE, Rogers JC (1979) The fast ice regimes of the Beaufort and Chukchi Sea coasts. Alaska. Cold Reg Sci Technol 1(2):129–152. https://doi.org/10.1016/0165-

232X(79)90006-5, https://www.sciencedirect.com/science/article/pii/0165232X79900065
Barthélemy A (2016) Representation of subgrid-scale sea ice-ocean interactions in large-scale models. Ph.D. Thesis, UCLouvain, Louvain-la-Neuve, http://hdl.handle.net/2078.1/171915
Barthélemy A, Fichefet T, Goosse H et al (2015) Modeling the interplay between sea ice formation and the oceanic mixed layer: limitations of simple brine rejection parameterizations. Ocean Model 86:141–152. https://doi.org/10.1016/j.ocemod.2014.12.009
Bitz CM, Lipscomb WH (1999) An energy-conserving thermodynamic model of sea ice. J Geophys Res Oceans 104(C7):15669–15677. https://doi.org/10.1029/1999jc900100
Blanke B, Delecluse P (1993) Variability of the tropical Atlantic Ocean simulated by a general circulation model with two different mixed-layer physics. J Phys Oceanogr 23(7):1363–1388. https://doi.org/10.1175/1520-0485(1993)023<1363:vottao>2.0.co;2
Bouchat A, Hutter N, Chanut J et al (2022) Sea Ice Rheology Experiment (SIREx) 1. Scaling and statistical properties of sea-ice deformation fields. J Geophys Res Oceans 127(4):e2021JC017667. https://doi.org/10.1029/2021JC017667
Bouchat A, Tremblay B (2017) Using sea-ice deformation fields to constrain the mechanical strength parameters of geophysical sea ice. J Geophys Res Oceans 122(7):5802–5825. https://doi.org/10.1002/2017JC013020, https://agupubs.onlinelibrary.wiley.com/doi/abs/10.1002/2017JC013020
Bouillon S, Morales Maqueda MÁ, Legat V et al (2009) An elastic-viscous-plastic sea ice model formulated on Arakawa B and C grids. Ocean Model 27(3–4):174–184. https://doi.org/10.1016/j.ocemod.2009.01.004
Bourassa MA, Gille ST, Bitz C et al (2013) High-latitude ocean and sea ice surface fluxes: challenges for climate research. Bull Am Meterol Soc 94(3):403–423. https://doi.org/10.1175/BAMS-D-11-00244.1 https://journals.ametsoc.org/view/journals/bams/94/3/bams-d-11-00244.1.xml
Bourgain P, Gascard JC (2011) The Arctic Ocean halocline and its interannual variability from 1997 to 2008. Deep-Sea Res I: Oceanogr Res Pap 58(7):745–756. https://doi.org/10.1016/j.dsr.2011.05.001, https://www.sciencedirect.com/science/article/pii/S0967063711000884
Brodeau L, Barnier B, Treguier AM et al (2010) An ERA40-based atmospheric forcing for global ocean circulation models. Ocean Model 31(3–4):88–104. https://doi.org/10.1016/j.ocemod.2009.10.005
Brown RD, Cote P (1992) Interannual variability of landfast ice thickness in the Canadian high Arctic, 1950–89. Arctic 45(3):273–284. https://doi.org/10.14430/arctic1402, http://www.jstor.org/stable/40511459
Carmack EC, Yamamoto-Kawai M, Haine TWN et al (2016) Freshwater and its role in the Arctic Marine System: sources, disposition, storage, export, and physical and biogeochemical consequences in the Arctic and global oceans. J Geophys Res Biogeosci 121(3):675–717. https://doi.org/10.1002/2015JG003140
Cavalieri D, Parkinson CL, Gloersen P et al (1996) Sea Ice Concentrations from Nimbus-7 SMMR and DMSP SSM/I-SSMIS Passive Microwave Data. Version 1
Coon MD, Knoke GS, Echert DC et al (1998) The architecture of an anisotropic elastic-plastic sea ice mechanics constitutive law. J Geophys Res Oceans 103(C10):21915–21925. https://doi.org/10.1029/98JC01259, https://www.agupubs.onlinelibrary.wiley.com/doi/abs/10.1029/98JC01259
Coon M (1980) A review of AIDJEX modeling. Sea Ice Processes and Models 12:25
Coon M, Kwok R, Levy G et al (2007) Arctic Ice Dynamics joint Experiment (AIDJEX) assumptions revisited and found inadequate. J Geophys Res Oceans 112(C11):1. https://doi.org/10.1029/2005JC003393
Courtois P, Hu X, Pennelly C et al (2017) Mixed layer depth calculation in deep convection regions in ocean numerical models. Ocean Model 120:60–78. https://doi.org/10.1016/j.ocemod.2017.10.007
Dai A, Trenberth KE (2002) Estimates of freshwater discharge from continents: latitudinal and seasonal variations. J Hydrometeorol 3(6):660–687. https://doi.org/10.1175/1525-7541(2002)003<0660:eofdfc>2.0.co;2
Dedrick KR, Partington K, Woert MV et al (2001) U.S. National/Naval ice center digital sea ice data and climatology. Can J Remote Sens 27(5):457–475. https://doi.org/10.1080/07038992.2001.10854887
Dee DP, Uppala SM, Simmons AJ et al (2011) The ERA-Interim reanalysis: configuration and performance of the data assimilation system. Q J R Meteorol Soc 137(656):553–597. https://doi.org/10.1002/qj.828
Depoorter MA, Bamber JL, Griggs JA et al (2013) Calving fluxes and basal melt rates of Antarctic ice shelves. Nature 502(7469):89–92. https://doi.org/10.1038/nature12567
Dethleff D, Loewe P, Kleine E (1998) The Laptev Sea flaw lead-Detailed investigation on ice formation and export during 1991/1992 winter season. Cold Reg Sci Technol 27(3):225–243. https://doi.org/10.1016/S0165-232X(98)00005-6
Divine D, Korsnes R, Makshtas A et al (2005) Atmospheric-driven state transfer of shore-fast ice in the northeastern Kara Sea. J Geophys Res Oceans 110(9):1–13. https://doi.org/10.1029/2004JC002706
Dmitrenko IA, Rudels B, Kirillov SA et al (2015) Atlantic water flow into the Arctic Ocean through the St. Anna Trough in the northern Kara Sea. J Geophys Res Oceans 120(7):5158–5178. https://doi.org/10.1002/2015JC010804, https://agupubs.onlinelibrary.wiley.com/doi/abs/10.1002/2015JC010804
Docquier D, Massonnet F, Barthélemy A et al (2017) Relationships between Arctic sea ice drift and strength modelled by NEMO-LIM3.6. Cryosphere 11(6):2829–2846. https://doi.org/10.5194/tc-11-2829-2017
Dumont D, Gratton Y, Arbetter TE (2009) Modeling the dynamics of the North Water Polynya ice bridge. J Phys Oceanogr 39(6):1448–1461. https://doi.org/10.1175/2008jpo3965.1
Dupont F, Dumont D, Lemieux JF et al (2022) A probabilistic seabed-ice keel interaction model. Cryosphere 16(5):1963–1977. https://doi.org/10.5194/tc-16-1963-2022, https://tc.copernicus.org/articles/16/1963/2022/
Dussin R, Barnier B, Brodeau L, et al (2016) The making of the DRAKKAR Forcing Set DFS5. DRAKKAR/MyOcean Report 01-04-16, LGGE, Grenoble, France
Fetterer F, Fowler C (2006) National Ice Center Arctic Sea Ice Charts and Climatologies in Gridded Format. Version 1
Haas C, Dierking W, Busche T, et al (2005) Envisat ASAR monitoring of polynya processes and sea ice production in the Laptev Sea. In: Proceedings, ESA Envisat Symposium, Salzburg, September 2004
Haine TWN, Martin T (2017) The Arctic-Subarctic sea ice system is entering a seasonal regime: implications for future Arctic amplification. Sci Rep 7(1):4618. https://doi.org/10.1038/s41598-017-04573-0
Heuzé C, Zanowski H, Karam S et al (2023) The deep Arctic Ocean and Fram Strait in CMIP6 models. J Clim 36(8):2551–2584. https://doi.org/10.1175/JCLI-D-22-0194.1, https://journals.ametsoc.org/view/journals/clim/36/8/JCLI-D-22-0194.1.xml, place: Boston MA, USA Publisher: American Meteorological Society
Hibler W (1979) A dynamic thermodynamic sea ice model. J Phys Oceanogr 9(4):815–846. https://doi.org/10.1175/1520-0485(1979)009<0815:adtsim>2.0.co;2
Hibler W, Schulson E (2000) On modeling the anisotropic failure and flow of flawed sea ice. J Geophys Res Oceans 105(C7):17105–17120. https://doi.org/10.1029/2000jc900045

Holloway G, Dupont F, Golubeva E et al (2007) Water properties and circulation in Arctic Ocean models. J Geophys Res Oceans 112(C4):1. https://doi.org/10.1029/2006JC003642, https://agupubs.onlinelibrary.wiley.com/doi/abs/10.1029/2006JC003642

Hunke EC, Dukowicz JK (1997) An elastic-viscous-plastic model for sea ice dynamics. J Phys Oceanogr 27(9):1849–1867. https://doi.org/10.1175/1520-0485(1997)027<1849:aevpmf>2.0.co;2

Huot PV (2021) Influence of small-scale processes on ocean-cryosphere-atmosphere interactions off Adélie Land, East Antarctica. Ph.D. Thesis, UCLouvain, Louvain-la-Neuve, http://hdl.handle.net/2078.1/254421

Hutter N, Bouchat A, Dupont F et al (2022) Sea Ice Rheology Experiment (SIREx): 2. Evaluating linear kinematic features in high-resolution sea ice simulations. J Geophys Res Oceans 127(4):e2021JC017666. https://doi.org/10.1029/2021JC017666

Ilıcak M, Drange H, Wang Q et al (2016) An assessment of the Arctic Ocean in a suite of interannual CORE-II simulations. Part III: Hydrography and fluxes. Ocean Model 100:141–161. https://doi.org/10.1016/j.ocemod.2016.02.004, https://www.sciencedirect.com/science/article/pii/S1463500316000238

Ip CF, Hibler WD, Flato GM (1991) On the effect of rheology on seasonal sea-ice simulations. Ann Glaciol 15:17–25. https://doi.org/10.3189/1991AoG15-1-17-25

Itkin P, Losch M, Gerdes R (2015) Landfast ice affects the stability of the Arctic halocline: evidence from a numerical model. J Geophys Res Oceans 120(4):2622–2635. https://doi.org/10.1002/2014jc010353

Iwamoto K, Ohshima KI, Tamura T (2014) Improved mapping of sea ice production in the Arctic Ocean using AMSR-E thin ice thickness algorithm. J Geophys Res Oceans 119(6):3574–3594. https://doi.org/10.1002/2013JC009749, https://agupubs.onlinelibrary.wiley.com/doi/abs/10.1002/2013JC009749

Janout MA, Hölemann J, Laukert G et al (2020) On the variability of stratification in the freshwater-influenced Laptev Sea Region. Front Mar Sci 7

König Beatty C, Holland DM (2010) Modeling landfast sea ice by adding tensile strength. J Phys Oceanogr 40(1):185–198. https://doi.org/10.1175/2009jpo4105.1

König Beatty C (2007) Arctic landfast sea ice. Ph.D. Thesis, New York University

Kwok R (2018) Arctic sea ice thickness, volume, and multiyear ice coverage: losses and coupled variability (1958–2018). Environ Res Lett 13(10):105005. https://doi.org/10.1088/1748-9326/aae3ec

Lecomte O, Fichefet T, Flocco D et al (2015) Interactions between wind-blown snow redistribution and melt ponds in a coupled ocean-sea ice model. Ocean Model 87:67–80. https://doi.org/10.1016/j.ocemod.2014.12.003, https://www.sciencedirect.com/science/article/pii/S1463500314001784

Lemieux J, Tremblay L, Dupont F et al (2015) A basal stress parameterization for modeling landfast ice. J Geophys Res Oceans 120(4):3157–3173. https://doi.org/10.1002/2014jc010678

Lemieux J, Dupont F, Blain P et al (2016) Improving the simulation of landfast ice by combining tensile strength and a parameterization for grounded ridges. J Geophys Res Oceans 121(10):7354–7368. https://doi.org/10.1002/2016jc012006

Lemieux J, Lei J, Dupont F et al (2018) The impact of tides on simulated landfast ice in a pan-Arctic ice-ocean model. J Geophys Res Oceans. https://doi.org/10.1029/2018jc014080

Lind S, Ingvaldsen RB, Furevik T (2018) Arctic warming hotspot in the northern Barents Sea linked to declining sea-ice import. Nat Clim Change 8(7):634–639. https://doi.org/10.1038/s41558-018-0205-y

Lin P, Pickart RS, Våge K et al (2021) Fate of Warm Pacific Water in the Arctic Basin. Geophys Res Lett 48(20):e2021GL094693. https://doi.org/10.1029/2021GL094693, https://agupubs.onlinelibrary.wiley.com/doi/abs/10.1029/2021GL094693

Lipatov MA, Volkov VA, May RI (2021) Linear trends in sea ice drift fields in the Arctic Ocean. Oceanology 61(3):297–304. https://doi.org/10.1134/S0001437021030073

Lipscomb WH, Hunke EC, Maslowski W et al (2007) Ridging, strength, and stability in high-resolution sea ice models. J Geophys Res Oceans 112(C3). https://doi.org/10.1029/2005JC003355, https://agupubs.onlinelibrary.wiley.com/doi/abs/10.1029/2005JC003355

Liu Y, Losch M, Hutter N et al (2022) A new parameterization of coastal drag to simulate landfast ice in deep marginal seas in the Arctic. J Geophys Res Oceans 127(6):e2022JC018413. https://doi.org/10.1029/2022JC018413, https://agupubs.onlinelibrary.wiley.com/doi/abs/10.1029/2022JC018413

Li Z, Zhao J, Su J et al (2020) Spatial and temporal variations in the extent and thickness of arctic landfast ice. Remote Sensing 12(1). https://doi.org/10.3390/rs12010064, https://www.mdpi.com/2072-4292/12/1/64

Locarnini RA, Mishonov AV, Antonov JI, et al (2013) World ocean atlas 2013. Vol 1, Temperature. National Oceanographic Data Center (US), Ocean Climate Laboratory https://doi.org/10.7289/V55X26VD, https://repository.library.noaa.gov/view/noaa/14847

Lorenz EN (1955) Available Potential Energy and the Maintenance of the General Circulation. Tellus 7(2):157–167. publisher: Taylor & Francis https://doi.org/10.3402/tellusa.v7i2.8796

Madec G, Imbard M (1996) A global ocean mesh to overcome the North Pole singularity. Clim Dyn 12(6):381–388. https://doi.org/10.1007/bf00211684

Madec G, Bourdallé-Badie R, Bouttier PA et al (2017) NEMO ocean engine. Zenodo

Mahoney AR, Eicken H, Gaylord AG et al (2014) Landfast sea ice extent in the Chukchi and Beaufort Seas: the annual cycle and decadal variability. Cold Reg Sci Technol 103:41–56. https://doi.org/10.1016/j.coldregions.2014.03.003

Mahoney A, Eicken H, Gaylord AG et al (2007) Alaska landfast sea ice: links with bathymetry and atmospheric circulation. J Geophys Res 112(C2). https://doi.org/10.1029/2006jc003559

Maslanik J, Stroeve J, Fowler C et al (2011) Distribution and trends in Arctic sea ice age through spring 2011. Geophys Res Lett 38(13):n/a. https://doi.org/10.1029/2011gl047735

Massonnet F, Barthélemy A, Worou K et al (2019) On the discretization of the ice thickness distribution in the NEMO3.6-LIM3 global ocean-sea ice model. Geosci Model Dev 12(8):3745–3758. https://doi.org/10.5194/gmd-12-3745-2019

Ma B, Steele M, Lee CM (2017) Ekman circulation in the Arctic Ocean: beyond the Beaufort Gyre. J Geophys Res Oceans 122(4):3358–3374. https://doi.org/10.1002/2016JC012624, https://agupubs.onlinelibrary.wiley.com/doi/abs/10.1002/2016JC012624

Meneghello G, Marshall J, Campin JM et al (2018) The ice-ocean Governor: ice-ocean stress feedback limits Beaufort Gyre spin-up. Geophys Res Lett 45(20):11,293-11,299. https://doi.org/10.1029/2018GL080171, https://agupubs.onlinelibrary.wiley.com/doi/abs/10.1029/2018GL080171

Meneghello G, Marshall J, Timmermans ML et al (2018) Observations of seasonal upwelling and downwelling in the Beaufort sea mediated by sea ice. J Phys Oceanogr 48(4):795–805. https://doi.org/10.1175/JPO-D-17-0188.1, https://journals.ametsoc.org/view/journals/phoc/48/4/jpo-d-17-0188.1.xml

Meredith M, Sommerkorn M, Cassotta S, et al (2019) Polar Regions. In: Pörtner HO, Roberts DC, Masson-Delmotte V, et al (eds) IPCC Special Report on the Ocean and Cryosphere in a Changing Climate. Cambridge University Press, UK and New York, USA, p 203–320, https://doi.org/10.1017/9781009157964.005 https://www.ipcc.ch/site/assets/uploads/sites/3/2022/03/05_SROCC_Ch03_FINAL.pdf

Merino N, Sommer JL, Durand G et al (2016) Antarctic icebergs melt over the Southern Ocean: climatology and impact on sea ice. Ocean Model 104:99–110. https://doi.org/10.1016/j.ocemod.2016.05.001

Metzner EP, Salzmann M, Gerdes R (2020) Arctic Ocean surface energy flux and the cold Halocline in future climate projections. J Geophys Res Oceans 125(2):e2019JC015554. https://doi.org/10.1029/2019JC015554, https://agupubs.onlinelibrary.wiley.com/doi/abs/10.1029/2019JC015554

Miller PA, Laxon SW, Feltham DL (2005) Improving the spatial distribution of modeled Arctic sea ice thickness. Geophys Res Lett 32(18):n/a. https://doi.org/10.1029/2005gl023622

Morales Maqueda MÁ, Willmott AJ, Biggs NRT (2004) Polynya dynamics: a review of observations and modeling. Rev Geophys 42(1). https://doi.org/10.1029/2002rg000116

Nguyen AT, Menemenlis D, Kwok R (2009) Improved modeling of the Arctic halocline with a subgrid-scale brine rejection parameterization. J Geophys Res Oceans 114(C11). https://doi.org/10.1029/2008JC005121, https://agupubs.onlinelibrary.wiley.com/doi/abs/10.1029/2008JC005121

Olason E (2016) A dynamical model of Kara Sea land-fast ice. J Geophys Res Oceans 121(5):3141–3158. https://doi.org/10.1002/2016jc011638

Olason E, Notz D (2014) Drivers of variability in Arctic sea-ice drift speed. J Geophys Res Oceans 119. https://doi.org/10.1002/2014JC009897

Orval T (2021) Sur la représentation de la glace de rive arctique dans le modèle NEMO3.6-LIM3. Master's thesis, Faculté des sciences, Université catholique de Louvain, Louvain-la-Neuve, http://hdl.handle.net/2078.1/thesis:30711

Peralta-Ferriz C, Woodgate RA (2015) Seasonal and interannual variability of pan-Arctic surface mixed layer properties from 1979 to 2012 from hydrographic data, and the dominance of stratification for multiyear mixed layer depth shoaling. Prog Oceanog 134:19–53. https://doi.org/10.1016/j.pocean.2014.12.005, https://www.sciencedirect.com/science/article/pii/S0079661114002158

Pickart RS (2004) Shelfbreak circulation in the Alaskan Beaufort Sea: Mean structure and variability. J Geophys Res Oceans 109(C4). https://doi.org/10.1029/2003JC001912, https://agupubs.onlinelibrary.wiley.com/doi/abs/10.1029/2003JC001912

Pickart RS, Weingartner TJ, Pratt LJ et al (2005) Flow of winter-transformed Pacific water into the Western Arctic. The Western Arctic Shelf-Basin Interactions (SBI) Project 52(24):3175–3198. https://doi.org/10.1016/j.dsr2.2005.10.009, https://www.sciencedirect.com/science/article/pii/S096706450500216X

Polyakov IV, Rippeth TP, Fer I et al (2020) Weakening of cold Halocline layer exposes sea ice to oceanic heat in the Eastern Arctic Ocean. J Clim 33(18):8107–8123. https://doi.org/10.1175/JCLI-D-19-0976.1, https://journals.ametsoc.org/view/journals/clim/33/18/jcliD190976.xml

Polyakov IV, Pnyushkov AV, Alkire MB et al (2017) Greater role for Atlantic inflows on sea-ice loss in the Eurasian Basin of the Arctic Ocean. Science 356(6335):285–291. https://doi.org/10.1126/science.aai8204

Polyakov IV, Pnyushkov AV, Carmack EC (2018) Stability of the arctic halocline: a new indicator of arctic climate change. Environ Res Lett 13(12). https://doi.org/10.1088/1748-9326/aaec1e

Prather MJ (1986) Numerical advection by conservation of second-order moments. J Geophys Res 91(D6):6671. https://doi.org/10.1029/jd091id06p06671

Preußer A, Heinemann G, Willmes S et al (2016) Circumpolar polynya regions and ice production in the Arctic: results from MODIS thermal infrared imagery from 2002/2003 to 2014/2015 with a regional focus on the Laptev Sea. Cryosphere 10(6):3021–3042. https://doi.org/10.5194/tc-10-3021-2016, https://tc.copernicus.org/articles/10/3021/2016/

Rampal P, Weiss J, Marsan D (2009) Positive trend in the mean speed and deformation rate of Arctic sea ice, 1979–2007. J Geophys Res 114(C5). https://doi.org/10.1029/2008jc005066

Regan H, Lique C, Talandier C et al (2020) Response of Total and Eddy Kinetic Energy to the Recent Spinup of the Beaufort Gyre. J Phys Oceanogr 50(3):575–594. https://doi.org/10.1175/JPO-D-19-0234.1, https://journals.ametsoc.org/view/journals/phoc/50/3/jpo-d-19-0234.1.xml

Reimnitz E, Dethleff D, Nürnberg D (1994) Contrasts in Arctic shelf sea-ice regimes and some implications: Beaufort Sea versus Laptev Sea. 4th Int Conf Paleoceanogr 119(3):215–225. https://doi.org/10.1016/0025-3227(94)90182-1, https://www.sciencedirect.com/science/article/pii/0025322794901821

Rousset C, Vancoppenolle M, Madec G et al (2015) The Louvain-La-Neuve sea ice model LIM3.6: global and regional capabilities. Geosci Model Dev 8(10):2991–3005. https://doi.org/10.5194/gmd-8-2991-2015

Rudels B, Jones EP, Anderson LG, et al (1994) On the intermediate depth waters of the Arctic Ocean. In: The Polar Oceans and their role in shaping the global environment. American Geophysical Union (AGU), pp 33–46, https://doi.org/10.1029/GM085p0033 https://agupubs.onlinelibrary.wiley.com/doi/abs/10.1029/GM085p0033

Schweiger A, Lindsay R, Zhang J et al (2011) Uncertainty in modeled Arctic sea ice volume. J Geophys Res 116. https://doi.org/10.1029/2011jc007084

Selyuzhenok V, Krumpen T, Mahoney A et al (2015) Seasonal and interannual variability of fast ice extent in the southeastern Laptev Sea between 1999 and 2013. J Geophys Res Oceans 120(12):7791–7806. https://doi.org/10.1002/2015JC011135

Selyuzhenok V, Mahoney A, Krumpen T et al (2017) Mechanisms of fast-ice development in the south-eastern Laptev Sea: a case study for winter of 2007/08 and 2009/10. Polar Res 36(1):1411140. https://doi.org/10.1080/17518369.2017.1411140

Serreze MC, Meier WN (2018) The Arctic's sea ice cover: trends, variability, predictability, and comparisons to the Antarctic. Ann N Y Acad Sci 1436(1):36–53. https://doi.org/10.1111/nyas.13856

Steele M, Morley R, Ermold W (2001) PHC: a global ocean hydrography with a high-quality Arctic Ocean. J Clim 14(9):2079–2087. https://doi.org/10.1175/1520-0442(2001)014<2079:PAGOHW>2.0.CO;2

Steele M, Boyd T (1998) Retreat of the cold halocline layer in the Arctic Ocean. J Geophys Res Oceans 103(C5):10419–10435. https://doi.org/10.1029/98JC00580, https://agupubs.onlinelibrary.wiley.com/doi/abs/10.1029/98JC00580

Steele M, Morison J, Ermold W et al (2004) Circulation of summer Pacific halocline water in the Arctic Ocean. J Geophys Res Oceans 109(C2). https://doi.org/10.1029/2003JC002009, https://agupubs.onlinelibrary.wiley.com/doi/abs/10.1029/2003JC002009

Sterlin J, Fichefet T, Massonnet F et al (2021) Sensitivity of Arctic sea ice to melt pond processes and atmospheric forcing: a model study. Ocean Model 167:101872. https://doi.org/10.1016/j.ocemod.2021.101872, https://www.sciencedirect.com/science/article/pii/S1463500321001256

Sumata H, Gerdes R, Kauker F et al (2015) Empirical error functions for monthly mean Arctic sea-ice drift. J Geophys Res Oceans 120(11):7450–7475. https://doi.org/10.1002/2015jc011151

Szanyi S, Lukovich JV, Barber DG et al (2016) Persistent artifacts in the NSIDC ice motion data set and their implications for analysis. Geophys Res Lett 43(20):10800–10807. https://doi.org/10.1002/2016GL069799, https://agupubs.onlinelibrary.wiley.com/doi/abs/10.1002/2016GL069799

Tamura T, Ohshima KI (2011) Mapping of sea ice production in the Arctic coastal polynyas. J Geophys Res Oceans 116(C7). https://doi.

org/10.1029/2010JC006586, https://agupubs.onlinelibrary.wiley.com/doi/abs/10.1029/2010JC006586

Tandon NF, Kushner PJ, Docquier D et al (2018) Reassessing sea ice drift and its relationship to long-term Arctic sea ice loss in coupled climate models. J Geophys Res Oceans 123(6):4338–4359. https://doi.org/10.1029/2017jc013697

Thorndike AS, Rothrock DA, Maykut GA et al (1975) The thickness distribution of sea ice. J Geophys Res 80(33):4501–4513. https://doi.org/10.1029/jc080i033p04501

Timmermans ML, Proshutinsky A, Krishfield RA et al (2011) Surface freshening in the Arctic Ocean's Eurasian Basin: an apparent consequence of recent change in the wind-driven circulation. J Geophys Res 116. https://doi.org/10.1029/2011jc006975

Timmermans ML, Marshall J (2020) Understanding Arctic Ocean circulation: a review of ocean dynamics in a changing climate. J Geophys Res Oceans 125(4):e2018JC014378. https://doi.org/10.1029/2018JC014378

Timmermans ML, Toole J, Krishfield R (2018) Warming of the interior Arctic ocean linked to sea ice losses at the basin margins. Sci Adv 4(8):eaat6773. https://doi.org/10.1126/sciadv.aat6773

Tremblay LB, Hakakian M (2006) Estimating the sea ice compressive strength from satellite-derived sea ice drift and NCEP reanalysis data. J Phys Oceanogr 36(11):2165–2172. https://doi.org/10.1175/JPO2954.1

Tschudi M, Meier WN, Stewart JS et al (2019) Polar Pathfinder Daily 25 km EASE-Grid Sea Ice Motion Vectors. Version 4:1

Untersteiner N (1975) Sea ice and ice sheets and their role in climatic variations. WMO The Phys Basis of Climate and Climate Modelling p 206-224(SEE N 76-19675 10-47)

Uotila P, Holland DM, Morales Maqueda MÁ et al (2006) An energy-diagnostics intercomparison of coupled ice-ocean Arctic models. Ocean Model 11(1):1–27. https://doi.org/10.1016/j.ocemod.2004.11.003, https://www.sciencedirect.com/science/article/pii/S1463500304000976

Uppala SM, Kållberg PW, Simmons AJ et al (2005) The ERA-40 re-analysis. Q J R Meteorol Soc 131(612):2961–3012. https://doi.org/10.1256/qj.04.176

Van Achter G, Fichefet T, Goosse H et al (2022) Modelling landfast sea ice and its influence on ocean-ice interactions in the area of the Totten Glacier. East Antarctica. Ocean Model 169:101920. https://doi.org/10.1016/j.ocemod.2021.101920, https://www.sciencedirect.com/science/article/pii/S1463500321001712

Vancoppenolle M, Fichefet T, Goosse H et al (2009) Simulating the mass balance and salinity of Arctic and Antarctic sea ice. 1. Model description and validation. Ocean Model 27(1–2):33–53. https://doi.org/10.1016/j.ocemod.2008.10.005

Vancoppenolle M, Bitz CM, Fichefet T (2007) Summer landfast sea ice desalination at point Barrow, Alaska: modeling and observations. J Geophys Res 112(C4). https://doi.org/10.1029/2006jc003493

Wang K (2007) Observing the yield curve of compacted pack ice. J Geophys Res Oceans 112(C5). https://doi.org/10.1029/2006JC003610, https://agupubs.onlinelibrary.wiley.com/doiabs/10.1029/2006JC003610

Weingartner TJ, Cavalieri DJ, Aagaard K et al (1998) Circulation, dense water formation, and outflow on the northeast Chukchi shelf. J Geophys Res Oceans 103(C4):7647–7661. https://doi.org/10.1029/98JC00374

WMO (1970) Sea-ice nomenclature, terminology, codes and illustrated glossary. Tech. Rep. WMO/OMM/BMO 259, WMO

Yu Y, Stern H, Fowler C et al (2014) Interannual variability of arctic landfast ice between 1976 and 2007. J Clim 27(1):227–243. https://doi.org/10.1175/jcli-d-13-00178.1

Zhang J, Rothrock DA (2003) Modeling global sea ice with a thickness and Enthalpy distribution model in generalized curvilinear coordinates. Mon Weather Rev 131(5):845–861. https://doi.org/10.1175/1520-0493(2003)131<0845:mgsiwa>2.0.co;2

Zhang J, Rothrock DA (2005) Effect of sea ice rheology in numerical investigations of climate. J Geophys Res Oceans 110(C8). https://doi.org/10.1029/2004JC002599, https://agupubs.onlinelibrary.wiley.com/doi/abs/10.1029/2004JC002599

Zweng MM, Reagan JR, Antonov JI, et al (2013) World ocean atlas 2013. Volume 2, Salinity. National Oceanographic Data Center (US), Ocean Climate Laboratory. https://doi.org/10.7289/V5251G4D, https://repository.library.noaa.gov/view/noaa/14848